The Geological Society

ES3 Earth Science, Systems and Society

ORIGINAL RESEARCH
published: 04 October 2021
doi: 10.3389/esss.2021.10039

From Continent to Ocean: Investigating the Multi-Element and Precious Metal Geochemistry of the Paraná-Etendeka Large Igneous Province Using Machine Learning Tools

J. J. Lindsay[1]*, H. S. R. Hughes[1], C. M. Yeomans[1], J. C. Ø. Andersen[1] and I. McDonald[2]

[1]Camborne School of Mines, University of Exeter, Cornwall, United Kingdom, [2]School of Earth and Ocean Sciences, Main College, Cardiff University, Cardiff, United Kingdom

Large Igneous Provinces, and by extension the mantle plumes that generate them, are frequently associated with platinum-group element (PGE) ore deposits, yet the processes controlling the metal budget in plume-derived magmas remains debated. In this paper, we present a new whole-rock geochemical data set from the 135 Ma Paraná-Etendeka Large Igneous Province (PELIP) in the South Atlantic, which includes major and trace elements, PGE, and Au concentrations for onshore and offshore lavas from different developmental stages in the province, which underwent significant syn-magmatic continental rifting from 134 Ma onwards. The PELIP presents an opportunity to observe magma geochemistry as the continent and sub-continental lithospheric mantle (SCLM) are progressively removed from a melting environment. Here, we use an unsupervised machine learning approach (featuring the PCA, t-SNE and *k*-means clustering algorithms) to investigate the geochemistry of a set of (primarily basaltic) onshore and offshore PELIP lavas. We test the hypothesis that plume-derived magmas can scavenge precious metals including PGE from the SCLM and explore how metal concentrations might change the metal content in intraplate magmas throughout rifting. Onshore lavas on the Etendeka side of the PELIP are classified as the products of deep partial melts of the mantle below the African craton but without significant PGE enrichment. Offshore lavas on both continents exhibit similarities through the multi-element space to their onshore equivalents, but they again lack PGE enrichment. Of the four onshore lava types on the Paraná side of the PELIP, the Type 1 (Southern) and Type 1 (Central-Northern) localities exhibit separate PGE-enriched assemblages (Ir-Ru-Rh and Pd-Au-Cu, respectively). It follows that there is a significant asymmetry to the metallogenic character of the PELIP, with enrichment focused specifically on lavas from the South American continent edge in Paraná. This asymmetry contrasts with the North Atlantic Igneous Province (NAIP), a similar geodynamic environment in which continent-edge lavas are also PGE-enriched, albeit on both sides of the plume-rift system. We conclude that, given the similarities in PGE studies of plume-rift environments, SCLM incorporation under progressively shallowing (i.e., rifting) asthenospheric conditions promotes the acquisition of metasomatic and residual PGE-bearing minerals, boosting the magma metal budget.

Keywords: plume, PGE, mantle, geochemistry, machine learning

OPEN ACCESS

Edited by:
Richard Palin,
University of Oxford, United Kingdom

Reviewed by:
Kim Cone,
Colorado School of Mines, United States
Alex Lipp,
Imperial College London, United Kingdom

***Correspondence:**
J. J. Lindsay
jordan@minviro.com

Received: 18 January 2021
Accepted: 03 September 2021
Published: 04 October 2021

Citation:
Lindsay J, Hughes HSR, Yeomans CM, Andersen JØ and McDonald I (2021) From Continent to Ocean: Investigating the Multi-Element and Precious Metal Geochemistry of the Paraná-Etendeka Large Igneous Province Using Machine Learning Tools. Earth Sci. Syst. and Soc. 1:10039. doi: 10.3389/esss.2021.10039

INTRODUCTION

Mantle Plumes and Precious Metals

Near-surface intrusive Ni-Cu-PGE deposits are famously located in the Noril'sk Talnakh intrusion in Siberia (e.g., Lightfoot, 2007), the Skaergaard Complex in Greenland (e.g., Andersen et al., 1998), and the Bushveld Complex in South Africa (e.g., Maier and Groves, 2011), as reviewed by Naldrett (1997) and Barnes et al. (2016). These locations share a similar geodynamic setting, with intraplate magmas interacting with thick, stable (i.e., older) continental crust, and this setting may directly influence the precious metal budget of magmas in this geodynamic context (e.g., Zhang et al., 2008; Maier and Groves, 2011).

Mantle plumes, buoyant diapirs made from the material of the mantle, can rise to the base of the lithosphere, introducing a thermal anomaly and inducing partial melting at the base of the asthenosphere, generating intraplate magmas (e.g., Morgan, 1971; Morgan, 1972; Griffiths and Campbell, 1990; Kellogg and King, 1993; Shannon and Agee, 1998; Jellinek and Manga, 2004). Intraplate magmas are thought to be sourced from a range of asthenospheric mantle reservoirs, many of which are relatively undepleted in incompatible elements (Zindler and Hart, 1986; Hawkesworth et al., 1988; Stracke et al., 2005; Hawkesworth and Scherstén, 2007). Furthermore, studies highlight the sub-continental lithospheric mantle (SCLM) below cratons as a potential source of metals, indicating that plume-derived magmas that ascend through the Archaean lithosphere are enriched in precious metals compared to those that do not feature significant lithospheric interaction (e.g., Hawkesworth and Scherstén, 2007; Zhang et al., 2008; Bierlein et al., 2009; Begg et al., 2010; Griffin et al., 2013; Barnes et al., 2015). This is particularly evident in regions in which the SCLM has been significantly pre-enriched by successive metasomatic events throughout their tectonic development (e.g., Wilson et al., 1996; Handler and Bennett, 1999; Powell and O'Reilly, 2007; Tassara et al., 2017; Rielli et al., 2018; Holwell et al., 2019; Wang Z. et al., 2020).

Our study looks at the nature of precious metal (PGE and Au) variations in plume-derived magmas, generated by the Southern Atlantic Tristan plume, alongside a large suite of major and trace element concentrations. For the past ~135 Myr, the environment above the Tristan plume has transitioned from a continental to oceanic setting, effectively removing the availability of the SCLM reservoir during melting and/or contamination. Herein, we investigate the effects this substantial geodynamic shift had on the relative concentrations of precious metals (i.e., the metal basket) in magmas generated in the region with a focus on correlations with major and trace element variability and the geochemical processes implied therein. Flood basalts can often share chalcophile, siderophile, and incompatible trace element signatures with underlying Ni-Cu-PGE mineralised magmatic intrusions, as exhibited in the PGE-rich East Greenlandic lavas near Skaergaard (e.g., Momme et al., 2002; 2006) and S-saturated Siberian Traps near Noril'sk (e.g., Ripley et al., 2003; Lightfoot and Keays, 2005). This connection has not been explicitly investigated in the flood basalts associated with the Tristan plume in this context, and our study aims to provide insight into the PGE mineralisation potential of magmas in the region.

We use an integrated machine learning approach based on work from Lindsay et al. (2021a) to analyse our new whole-rock geochemical data suite from onshore and offshore Tristan plume lavas, which comprise the Paraná-Etendeka Large Igneous Province (PELIP). Bulk geochemical data sets are excellent candidates for exploration using machine learning algorithms (MLAs), often comprising upwards of 50 measured elemental concentrations and hundreds of samples. This method allows us to explore multi-element trends and relationships that typically go undetected using traditional geochemical two-variable plots. By comparing and contrasting our new data to the North Atlantic Igneous Province (NAIP), which shares a similar plume-rift geodynamic setting to the Tristan plume, and was the focus of the workflow in Lindsay et al. (2021a), we work towards a multi-element variability model for plume metallogenesis in the Atlantic Ocean.

The Paraná-Etendeka Large Igneous Province

The PELIP is preserved asymmetrically between (primarily) Brazil in South America, and (to a lesser extent) Namibia in Africa, with a 15 times greater volume of lavas found in South America (around 1.2×10^6 km^2; Fodor et al., 1989). The lavas range in composition from basalts through to rhyolites, and, even amongst the mafic rocks, there is geochemical evidence for multiple mantle sources (e.g., Le Roux et al., 2002; Gibson et al., 2005; Beccaluva et al., 2020). After the Tristan plume arrived at the Gondwanan lithosphere under the modern-day central Paraná region in Brazil ca. 135 Ma, it induced partial melting of the asthenosphere and erupted lava at a rate of 0.8 km^3/year (Renne et al., 1996). These early Tristan lavas were primarily basaltic and were compositionally zoned into High-Ti in central and north-west Paraná, and Low-Ti in the south-east, the latter of which eventually progressed into bimodal mafic-felsic volcanism (Peate et al., 1992; Polo et al., 2018).

Currently found at the centre of the southern Atlantic Ocean, the Tristan plume lay beneath the South American and African Plate throughout the Cretaceous and Cenozoic eras (e.g., Douglass et al., 1999; Gibson et al., 2005; Fromm et al., 2015). The plume is responsible for the eruption of the lavas of PELIP, one of the largest continental flood basalt (CFB) provinces in the world (e.g., Stewart et al., 1996; Courtillot et al., 2003; Gibson et al., 2005). After Gondwana rifted (e.g., de Wit et al., 2008; Jokat and Reents, 2017; Martins-Ferreira et al., 2020), the plume produced volcanics in the newly opened ocean, creating the seafloor Rio Grande Rise and Walvis Ridge topographic features (e.g., O'Connor and Duncan, 1990; Ussami et al., 2013) (as shown in **Figure 1A**).

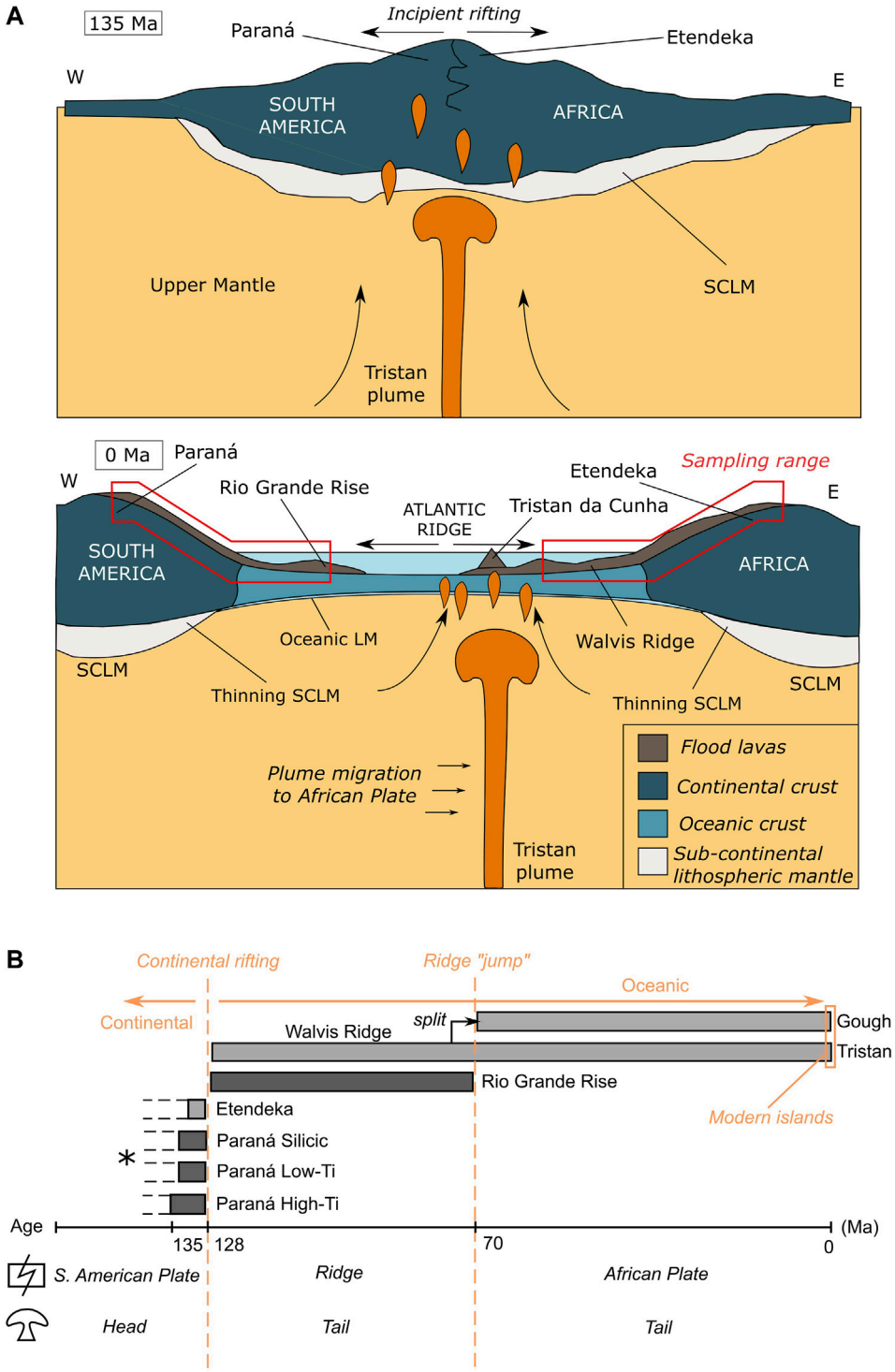

FIGURE 1 | (A) Schematic two-part cross-section of the formation of the southern Atlantic Ocean, detailing the arrival of the Tristan plume beneath Gondwanan lithosphere 135–128 Ma, melting of the asthenosphere and SCLM, incipient continental rifting beginning after 128 Ma, and the eventual formation of oceanic hotspot trails connected to the plume until 0 Ma. The sample range for this study is indicated by the red boxes (refer to **Table 1**). lithospheric mantle (oceanic). **(B)** Schematic timeline for the PELIP, showing the eruption scales for each major locality from 135 Ma to present and major tectonic events such as rifting at 128 Ma and the ridge-jump at 70 Ma. Also included are the plate position of the plume focus and the head-to-tail plume transition. (* = although dated primarily between 135 and 128 Ma, the large majority of onshore lavas erupted between 135 and 134 Ma on the Paraná side).

From 134 to 128 Ma (Stewart et al., 1996), rifting initiated in the thermally thinned and weakened lithosphere (McKenzie and White, 1989; Turner et al., 1996), like north-westerly plate movement, migrated the magmatic activity to the Etendeka-Angola margin, synchronous with the eruption of the south-eastern Low-Ti lavas in Paraná (Beccaluva et al., 2020). Etendeka lavas are also sub-divided into High-Ti and Low-Ti groups and are bimodal throughout (Milner et al., 1995a; Marsh et al., 2001). Following significant extension and basin formation, as the South American and African continents drifted further apart, the Tristan plume continued to erupt lava on the newly-formed seafloor throughout the Cretaceous at a less productive volcanic flux given the transition from plume head to tail (Camboa and Rabinowitz, 1984; Gibson et al., 2005; Fromm et al., 2015). The plume-derived lavas formed ridges on either side of the mid-ocean ridge, the Rio Grande Rise on the Southern American plate, and the Walvis Ridge on the African plate, which connect the PELIP to the active hotspot focus (O'Connor and Duncan, 1990; O'Connor and Jokat, 2015; Homrighausen et al., 2019). **Figure 1B** summarises the PELIP timeline.

Geochemical Classification of the Paraná-Etendeka Large Igneous Province

Paraná

The predominantly basaltic and basaltic-andesitic lavas of the Paraná CFB sequence erupted onto the Botucatu Formation and Proterozoic basement of the late Gondwanan continent, peaking between 135 and 134 Ma but continuing to 128 Ma (e.g., Gordon, 1947; Leinz, 1949; Leinz et al., 1966; Peate et al., 1990; Marques et al., 1999; Thiede and Vasconcelos, 2010; Rocha-Júnior et al., 2012; Hartmann et al., 2019). Previous studies on the geochemistry of the Paraná lavas, referred to more formally as the Serra Geral Formation in Brazil, classified them based on major and trace element concentrations, and isotopic variations (e.g., Fodor 1987; Peate et al., 1992). The primarily tholeiitic High-Ti, Low-Ti, and Silicic groups present throughout the creation of the CFB were initially proposed by Fodor (1987) but later given more distinct magma-type subdivisions. The High-Ti group lavas are divided into three classifications: Urubici, the highest-Ti lavas in the Serra Geral Formation, and the Pitanga and Paranapanema lavas (Peate et al., 1992). Gramado and Esmeralda lavas, the two major Low-Ti group classifications, are often associated with the silicic Chapecó and Palmas members within the bimodality of south-eastern Low-Ti lavas in Paraná (Bellieni et al., 1984; Peate et al., 1990; Peate et al., 1992; Peate, 1997). Relatively scarce in the region compared to the other main lava types, the Ribeira lavas are primarily distinguished isotopically, forming intermediate lava with properties of both High-Ti and Low-Ti sub-groups (Peate et al., 1992; Peate and Hawkesworth, 1996). Licht (2018) further classified all mafic and silicic lavas in the region into 16 types based on Si, Ti, Zr, and P concentrations. In this new scheme, Gramado and Esmeralda comprise Type 1 (Southern), Ribeira and Paranapanema comprise Type 1 (Central-Northern), Pitanga and Urubici are Type 4, and Palmas and Chapecó belong to Types 9 and 14, respectively (Licht, 2018). The remaining 12 types are significantly less common volumetrically (Licht, 2018) and do not feature in this current study.

The literature supports the theory that the magma-types erupted in a synchronous manner from separate subsurface melt systems (Peate, 1997; Rämö et al., 2016; Beccaluva et al., 2020), with each system being subject to distinct differentiation processes and geochemical development (Turner et al., 1999; Rossetti et al., 2018).

Etendeka

The African equivalents of the Serra Geral lavas are dated consistently ~130 ± 2 Ma (by $^{40}Ar/^{39}Ar$ mineral dating as per Renne et al., 1996; Stewart et al., 1996), coinciding with the late-stage bimodal Paraná lavas and earliest Atlantic opening (Milner et al., 1995c). The Etendeka Group is distributed roughly parallel to the coastline, split into two mafic regions separated into northern and southern sections by Möwe Bay (Ewart et al., 1998a). The lavas collectively contribute a much smaller volume to the total preserved throughout the PELIP, covering ~80,000 km^2 (Erlank et al., 1984) or 6% of the preserved CFB area (Miller, 2008). The Etendeka Group Lavas, comprising basalts, basaltic-andesites, and andesites with quartz latites (Erlank et al., 1984; Marsh et al., 2001), overlie the mixed sedimentary/volcanic rocks of the Neoproterozoic Damara Sequence and the Mesozoic Karoo sediments (Miller, 2008 and references therein). Similar to Paraná, the northern region is dominated by High-Ti signatures and the southern region by Low-Ti lavas. Silicic lavas are typically located in the south, such as in the Goboboseb Mountains (Ewart et al., 1998b), and the province has many intrusive dolerite complexes (Milner et al., 1995c).

The Etendeka Group features two main geochemical sub-groups in the Tafelberg and Khumib, which represent the bulk of the Type 1 and Type 4 Serra Geral magma classifications, respectively (Erlank et al., 1984; Marsh et al., 2001; Ewart, 2004; Miller, 2008). Minor Esmeralda and Kuidas groups complete the Low-Ti components of the Etendeka Group Lavas (Ewart, 2004), showing slight trace element and isotopic differences to Tafelberg. Most noteworthy is the observation that the lavas and intrusive complexes in Etendeka generally have markedly higher MgO (15–25 wt.%; Teklay et al., 2020) than their equivalents in Serra Geral (typically <8 wt.%; Peate, 1997), representing a higher degree of partial melting and/or higher temperatures during melting in the former (Teklay et al., 2020). Consequently, the eastern part of the onshore PELIP is considered a more accurate record of the Tristan plume mantle source(s) signature through the Cretaceous (Hoernle et al., 2015; Jennings et al., 2019).

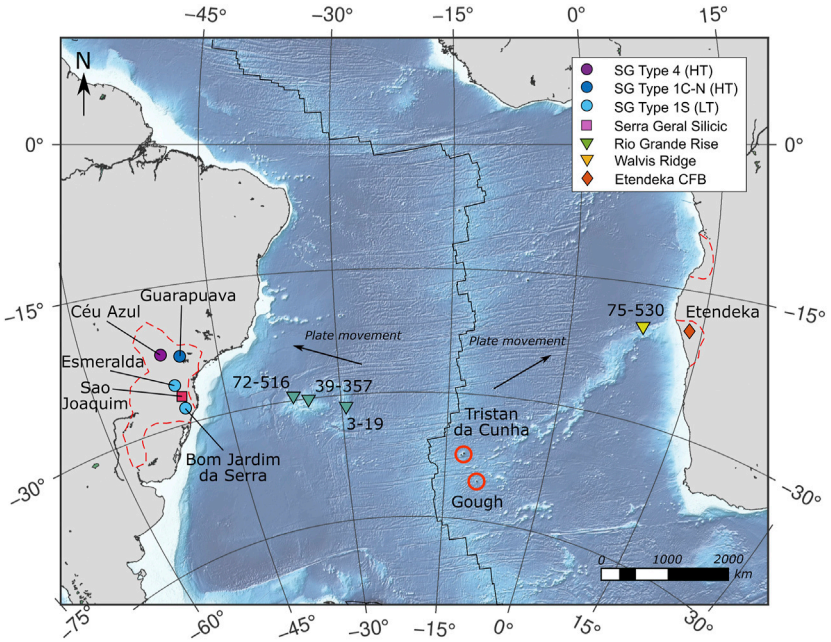

FIGURE 2 | Schematic map of eastern South America, western Africa, and the South Atlantic Ocean with ocean floor bathymetry, detailing the site localities for rock samples analysed in this study. Symbology is used throughout all plots related to these localities. For offshore samples, the IODP drill site and core numbers are displayed, and the current focus of the Tristan plume (beneath Tristan da Cunha and Gough) is shown in red solid circles. Also outlined onshore are the rough boundaries of the continental lavas in dashed red lines.

Rio Grande Rise and the Walvis Ridge

The formation of the age-progressive seafloor volcanic ridges in the developing South Atlantic Ocean ca. 128 Ma onwards resulted from a combination of mid-ocean ridge and intraplate magmatism following the breakup of Gondwana (O'Connor and Jokat, 2015; Homrighausen et al., 2019). The submarine ridges present the unusual situation in which OIB and MORB of the same age exist adjacent to each other, as normally plume lavas intersect much older oceanic crust in hotspots (e.g., Morgan, 1971; O'Connor and Duncan, 1990; Fromm et al., 2017). The Rio Grande Rise on the South American Plate has average bathymetries of 3,000 m in the west to 1,000 m in the central region (Camboa and Rabinowitz, 1984). Drill core samples from the plateau comprise mainly tholeiitic and alkali basalts (O'Connor and Duncan, 1990; Gibson et al., 2005). Working eastwards from the continent, the trail becomes significantly less prominent after 34°S 29°W (**Figure 2**). At this stage, the plume focus abruptly transitioned from the centre of the mid-ocean ridge to on top of the African Plate ca. 70 Ma (**Figure 1B**) (e.g., Camboa and Rabinowitz, 1984; Gibson et al., 2005; Fromm et al., 2015; O'Connor and Jokat, 2015; Graça et al., 2019).

The Walvis Ridge, on the African Plate, is of a similar age to the Rio Grande Rise (Milner et al., 1995c) and forms a narrow trail westwards from the High-Ti Khumib lava exposures in Namibia (Homrighausen et al., 2019). Bathymetric data places it at between 2,500 and 1,600 m below sea level, with the ridge increasing in height from east to west (Der Verfasser et al., 2011). At around 29°S 2°E, the trail bifurcates into two younger ridges, the Tristan and Gough tracks (O'Connor and Duncan, 1990; Rohde J. K. et al., 2013; Rohde J. et al., 2013), eponymous with the islands associated with the current plume focus (**Figure 2**). A significant jump in tectonic plate movement at ~70 Ma resulted in the splitting of the Walvis hotspot trail and the cessation of Rio Grande Rise volcanism, after which the Tristan plume focus lay to the east of the ridge for the first time, and volcanism occurred exclusively on the African plate (Rohde J. K. et al., 2013; Graça et al., 2019). Prior to the jumps, it is suggested that the two >70 Ma ridges would have been analogous with Iceland, as a contiguous volcanic ocean island formed by sustained ridge opening and addition of plume-derived lavas (Graça et al., 2019). The seafloor Walvis-Tristan-Gough hotspot track thus represents all stages of the transition from continental to modern-day oceanic plume.

MATERIALS AND METHODS

Samples

Table 1 displays sample information for our new PELIP suite (n = 116). Whole rock samples were collected for onshore fossil lavas in Paraná (n = 83). Etendeka samples (n = 10) were acquired from a collaborator, and represent the Low-Ti

TABLE 1 | Samples gathered in this study with the locality, formation (or drill core for offshore samples), rock type, and quantity (excluding duplicates). These samples are classified purely by geographic location at this stage, prior to geochemical analyses. Samples are listed west to east as per **Figure 2**. This represents the complete list of samples for the study, and some are omitted from final analyses as per *Machine Learning Workflow*.

Locality	Formation or drill core	Rock type	Quantity
Paraná Basalts (Northern)	Paranapanema, Pitanga, Urubici (HT)	Basalt	38
Paraná Basalts (Southern)	Gramado, Esmeralda (LT)	Basalt	39
Paraná Silicic	Chapecó (HT), Palmas (LT)	Dacite	6
Rio Grande Rise	DSDP Legs 3–19, 39–367, 72–516	Basalt	16 (4,4,8)
Walvis Ridge	DSDP Leg 75–530	Basalt	7
Etendeka	Tafelberg (LT)	Basalt	10
		Total	**116**

LT, low titanium; HT, high titanium; DSDP, deep sea drilling project.

end-members of the Namibian continental flood basalts (the Tafelberg Formation). Drill core samples (n = 23) were collected from the International Offshore Drilling Programme (IODP) repository in Bremen, Germany for offshore sites along the Rio Grande Rise (DSDP Leg 3–19, 39–357, and 72–516; n = 4, 4, and 8, respectively) and Walvis Ridge (DSDP Leg 75–530; n = 7). Given the higher degree of geochemical variability (e.g., Peate, 1997), volumetric abundance, and their potential to reflect sensitive changes in geodynamics, the Paraná rocks formed the bulk of the sample set in this study. For the present paper, we have classified Paraná samples based on their Si-Ti-Zr-P concentrations as suggested in Licht (2018), resulting in Serra Geral Type 1 (Southern), Type 1 (Central-Northern), Type 4, and Silicic groups.

To account for sample size differences (e.g., ~1 kg for Paraná lavas to ~50 g for IODP core sections) and potential geochemical heterogeneity within rock samples, randomly selected larger samples were cut into pieces equivalent in weight to core samples and processed individually as separate runs, i.e., sample A and B belonging to a single large original rock. The geochemistry of each was compared as a check on the processing methodology and as a comparison between samples of significantly different sizes from different localities. These A and B splits were then processed and analysed as separate samples, and their geochemistry was compared for quality control. Sample split details are available in **Supplementary Material A1**. **Figure 2** shows the general sample localities within the context of the Southern Atlantic, and **Table 1** gives a summary of sample localities, nomenclature and quantities. A full sample database with rock descriptions and physical properties is presented in **Supplementary Material A2**.

Laboratory Techniques

Rock samples were crushed to 1–2 mm chips using a jaw crusher following removal of weathered material and amygdales. They were then milled in a chrome-steel TEMA mill for use in bulk geochemical analysis techniques. Major elements were measured using X-ray fractionation (XRF) (using methods from Kystol and Larsen, 1999; Tegner et al., 2009). Dried and ignited samples were fused in a furnace in platinum crucibles with lithium borate flux, and cooled samples were moulded into beads using ammonium iodide as a wetting agent. Fused beads were analysed using a Bruker S4 Pioneer XRF spectrometer at Camborne School of Mines, alongside AGV-1, BHVO-2, BIR and DNC-1 standards. Trace elements were measured using inductively coupled plasma mass spectrometry (ICP-MS) at Camborne School of Mines (following the methodology of McDonald and Viljoen, 2006). This method used the 4-Acid sample dissolution technique before element detection using the Agilent 7700 Series mass spectrometer, alongside BCR-2 and Bir-1A standards.

Finally, Os, Ir, Ru, Rh, Pt, Pd, and Au were measured at Cardiff University using the Ni-S fire assay and tellurium co-precipitation technique for PGE analysis outlined by Huber et al. (2001) and McDonald and Viljoen (2006). For this method, 15 g of sample was mixed with 12 g of borax flux, 6 g $NaCO_3$, 0.9 g solid sulfur, 1.08 g Ni, and 1 g silica, and the mixture was melted in a furnace at 1,000 ˚C for 1.5 h. The sulfide bead segregated from the quenched silicate matrix was dissolved in hydrochloric acid, re-precipitated with Te, filtered and diluted. The final solutions were then analysed for precious metal concentrations using ICP-MS, alongside the TBD1 and WPR1 standards.

Full (anhydrous) major, trace and PGE+Au data are provided in Supplementary A1, with standard measurements, blank measurements (analytical and procedural), and detections limits where applicable.

Machine Learning Workflow

We have implemented the machine learning workflow introduced by Lindsay et al. (2021a) to examine the multi-element geochemistry of the PELIP and the Southern Atlantic plume-rift system. The workflow combines Principal Component Analysis (PCA) and t-Distributed Stochastic Neighbour Embedding (t-SNE) feature extraction methods with k-means clustering. All methods used algorithms from the *sci-kit learn v0.21.3* package for Python 3.7.4 (Pedregosa et al., 2011) in addition to *NumPy v1.16.5* (Harris et al., 2020) and *pandas v0.25.1* (McKinney, 2010) packages. All code used is available in **Supplementary Material B**.

Both PCA and t-SNE are effective dimensionality-reduction techniques that allow for the management of data sets with high dimensionality (i.e., a large number of variables/features). These techniques provide a means for digesting and presenting substantial amounts of variability information

contained within a large geochemical suite. By reducing the dimensionality of our data down to more manageable low-dimensional components we can effectively discuss complex multi-elemental trends. Principal components (PCs) generated during PCA, features that describe the directions of largest variability trends throughout the entire data structure (Pearson, 1901; Hotelling, 1933; Chang, 1983), can highlight inter-element associations, identify key drivers behind fluctuations in variable associations, and recognise multi-element enrichment signatures (Hyvärinen et al., 2001; Davis, 2002; Jolliffe, 2002). This information is generally displayed in "biplots," which illustrate both sample and element variability through the entire data set. The PCs can then be utilised in *k*-means clustering optimisation.

In comparison to PCA, the slightly more advanced, non-linear t-SNE method summarises the variability of all elements in a high dimensional data set by visualising this information in a single newly-generated low-dimensional space referred to as an embedding (van der Maaten and Hinton, 2008; van der Maaten, 2014). This technique uses the Kullback-Leibler Divergence (Kullback and Leibler, 1959) to preserve similarity between data points within high-dimensional space and transform this information into an embedding. This creates a summary "map" of cumulative sample variability across all included elements. The positions of data points within an embedding space are strongly indicative of how geochemically similar or different they are to other data points, although it should be noted that the high-dimensional similarity of proximal points is preserved better than dissimilarity between distal points (Baramurali et al., 2019). Individual element variability, sample classifications, and multi-element clusters recognised through PCA can be contextualised within the overall data structure in embeddings to quickly and efficiently describe a wealth of information for a complete data set. We work with three user-determined "hyperparameters" in our models: perplexity (the balance between portraying local and global trends in the data), learning rate (the increments taken to find the optimal embedding layout), and maximum iterations (the number of times the algorithm will try to optimise) (van der Maaten and Hinton, 2008).

We also use *k*-means clustering, an unsupervised MLA that clusters data into a pre-determined number of classification groups (*k*), based on an iterative density function that seeks out the optimum similarity between the data set across high-dimensional space (MacQueen, 1967; Howarth, 1983; Michie et al., 1994; Hastie et al., 2009; Marsland, 2009). This allows for objective classification using a multitude of variables, identification of multi-dimensional trends in the sample space and tests the similarity of previous classification clusters through the data structure. We can retrospectively assess clustering performance using the Davies-Bouldin Index (DBI) calculation (Davies and Bouldin, 1979), which highlights the statistically-optimum cluster number as a function of intra-cluster density. A low DBI is desirable and denotes a high degree of similarity between points in each cluster, and *k*-means models with the lowest DBI are prioritised in the study. Original data and Principal Components from PCA are used as inputs for *k*-means in this study, and the results are compared using DBI in pursuit of the most robust classification set-up. For an in-depth account of the MLA methodology, algorithm processes and review of the techniques within, refer to Lindsay et al. (2021a).

The techniques herein require data sets without zeroes or missing (blank) or non-numerical (e.g., below detection limit) entries. For this reason, despite being measured in some localities in our study, Te, W and Os were omitted from the working data set given the high volume of missing values. Further, BaO and Cr_2O_3 were removed from the XRF-derived data set as the concentrations of Ba and Cr were measured separately using the higher-precision ICP-MS technique, rendering the equivalent oxide values unnecessary. Rounded-zero imputation, as recommended by Horrocks et al. (2019), was not utilised in this instance to fill gaps in the data sheet. Finally, two Rio Grande Rise samples were removed from the data set due to anomalously high (~19 wt.%) loss-on-ignition (LOI) values, likely indicating a high degree of alteration of these basaltic samples. The final data set used in all MLA stages consisted of 116 lines (including additional data from A/B sample splits and duplicate analyses, minus omissions for the above conditions), with concentrations for 51 major element oxides and trace elements measured for each sample. The final processed data is available in **Supplementary Material A3**, alongside new PCA, t-SNE and *k*-means information discussed herein. Samples excluded for data analyses are not discussed further herein.

Since this data set is compositional in nature, standardisation of all measurements is required before any statistical analyses (Chayes, 1960; Palowsky-Glahn and Egozcue, 2006; Buccianti and Grunsky, 2014). Standardisation of data via the z-score calculation (Kreyszig, 1979) was performed on the data set prior to use in algorithms. The calculation presents all measured concentrations as a function of standard deviations from the mean value for each element. This validates the use of compositional data in this workflow and allows for a more accurate comparison of mixed-unit concentrations across the different methods used by eliminating bias from, for example, high numerical values for elements measured in ppm (e.g., Ni and Cu) compared to small values measured in ppb (e.g., PGE). This process of standardisation, either using z-scores or other similar calculations, is recommended for data treatment prior to most unsupervised learning MLAs (Taylor et al., 2010; Wang J. et al., 2020), and is used prior to all analyses in this paper. Element standard deviations (with other basic statistics) and z-scores are given next to raw concentrations in **Supplementary Materials A1, A3**, respectively.

TABLE 2 | Minimum, maximum, and mean (**x**) values for elemental concentrations measured for each locality in the PELIP, excluding Cr_2O_3, BaO, Te, and W. "-" not measured. * - summary stats use all sample data, including duplicates, (A) and (B) splits, and samples excluded from later MLA models for reasons discussed in *Machine Learning Workflow*.

	Etendeka (*n* = 12)*			**Rio grande rise (*n* = 15)***			**SG silicic (*n* = 7)***			**SG Type 1 (C-N) (*n* = 34)***			**SG Type 1 (S) (*n* = 52)***			**SG Type 4 (*n* = 25)***			**Walvis ridge (*n* = 9)***		
wt.%	**min**	**max**	**x**	**min**	**max**	**x**	**min**	**max**	**x**	**min**	**max**	**x**	**min**	**max**	**x**	**min**	**max**	**x**	**min**	**max**	**x**
LOI	0.1	1.0	0.4	2.4	19.0	6.5	0.6	1.3	0.9	0.1	1.4	0.5	0.0	3.5	0.8	0.3	0.9	0.7	1.6	2.8	2.2
SiO_2	45.5	52.6	49.3	40.9	51.5	48.2	64.3	69.7	67.3	50.1	51.7	50.9	50.0	60.7	53.1	50.1	54.0	51.0	49.2	49.9	49.5
Al_2O_3	9.6	15.7	13.4	8.5	19.5	14.7	12.6	13.5	13.0	12.2	13.8	12.8	12.5	16.9	13.8	11.6	13.4	12.6	14.8	16.1	15.6
Fe_2O_3	10.8	16.2	13.3	9.8	17.0	12.5	6.3	7.5	6.8	13.2	16.1	15.2	5.5	14.9	13.3	12.1	16.0	14.8	10.0	12.0	11.0
CaO	7.6	11.9	9.8	10.4	16.0	11.7	2.7	3.2	3.0	8.5	10.9	9.1	5.6	11.3	9.2	6.8	8.5	8.1	9.3	10.8	10.1
MgO	5.4	14.9	9.3	3.2	18.7	6.9	1.0	1.7	1.3	4.5	6.7	5.2	2.6	6.6	5.1	3.1	4.8	4.2	6.9	8.8	7.9
SO_3	0.06	0.09	0.08	0.07	0.55	0.14	0.01	0.07	0.05	0.01	0.01	0.01	0.01	0.12	0.07	0.01	0.08	0.03	0.08	0.18	0.12
Na_2O	1.46	2.63	2.25	1.95	3.05	2.64	2.77	3.66	3.24	2.18	2.90	2.50	2.10	4.54	2.57	2.40	2.91	2.65	2.78	3.20	2.98
K_2O	0.29	1.03	0.72	0.23	1.32	0.53	3.61	4.27	3.95	0.86	1.89	1.15	0.39	3.03	1.21	1.17	2.45	1.61	0.12	0.69	0.43
TiO_2	0.68	2.50	1.51	0.82	2.54	2.05	0.97	1.45	1.15	1.74	2.53	2.27	0.74	1.85	1.45	3.20	4.01	3.75	1.67	1.78	1.73
P_2O_5	0.08	0.33	0.18	0.08	0.75	0.30	0.27	0.46	0.34	0.19	0.32	0.27	0.14	0.29	0.20	0.50	1.00	0.61	0.26	0.32	0.28
MnO	0.17	0.23	0.18	0.13	0.24	0.18	0.11	0.15	0.12	0.19	0.23	0.22	0.08	0.35	0.20	0.14	0.24	0.19	0.21	0.30	0.25
Ppm																					
Sc	18	37	26	18	42	37	14	16	15	40	46	42	12	49	35	19	37	31	36	39	37
V	138	396	272	132	386	316	34	102	67	411	549	466	121	472	357	251	501	396	291	320	308
Cr	61	1,199	369	72	872	283	6	62	40	33	159	74	10	137	67	5	87	23	108	152	130
Co	35	87	54	42	84	50	10	14	11	46	61	52	20	60	43	32	51	44	32	44	40
Ni	37	776	238	35	408	108	1	133	28	40	86	57	11	124	52	11	81	35	58	75	65
Cu	31	198	97	37	620	262	8	345	138	156	393	257	44	547	204	138	338	217	95	229	139
As	0.5	1.7	1.1	2.5	35.0	9.7	0.4	120.7	21.5	0.5	0.6	0.5	0.2	66.5	10.0	0.4	24.1	2.6	2.4	8.6	4.7
Se	1.5	3.8	2.6	2.2	5.1	4.0	4.3	7.1	5.2	2.1	5.1	3.1	1.5	4.2	3.0	3.6	6.3	4.8	3.0	3.7	3.3
Rb	10	25	18	5	15	9	81	148	122	17	50	29	6	87	39	31	61	40	1	18	10
Sr	111	586	286	105	964	343	104	363	176	226	401	287	149	1,096	223	396	713	530	245	307	277
Y	17	30	22	15	40	31	34	61	44	23	41	35	12	42	30	30	56	41	27	33	31
Zr	58	156	110	31	185	146	241	702	381	121	208	183	86	212	138	242	441	300	119	129	125
Nb	4	16	7	1	73	15	19	61	32	5	17	13	4	15	9	9	38	20	16	18	18
Ba	74	457	224	7	703	199	531	1,087	723	267	398	332	115	721	293	532	755	586	105	155	126
La	7	29	15	1	59	19	36	74	47	17	27	23	9	35	19	39	61	43	13	16	15
Ce	17	60	32	3	112	40	71	146	94	35	57	49	20	73	41	83	141	94	30	35	33
Pr	2.3	7.6	4.2	0.7	12.0	5.2	8.9	20.4	12.3	4.6	7.2	6.4	2.7	8.8	5.2	10.9	17.4	12.1	3.8	4.5	4.2
Nd	9	31	18	4	45	23	34	82	48	19	30	27	12	34	21	45	74	51	18	20	19
Sm	2.4	6.9	4.4	1.8	6.9	5.5	7.2	16.8	10.4	4.4	7.0	6.3	3.5	7.3	5.1	9.8	15.7	10.9	4.3	4.9	4.6
Eu	0.8	2.3	1.5	0.8	2.3	1.9	1.5	4.6	2.5	1.5	2.2	2.0	1.3	1.9	1.5	3.0	4.8	3.4	1.5	1.7	1.6
Gd	3.0	6.8	4.9	2.8	7.9	6.2	7.1	15.8	9.9	4.8	8.0	7.1	4.2	7.7	5.7	9.3	15.3	10.8	4.9	5.8	5.5
Tb	0.5	0.9	0.7	0.5	1.2	0.9	1.1	2.2	1.4	0.7	1.2	1.1	0.5	1.2	0.9	1.2	2.1	1.5	0.8	0.9	0.8
Dy	3.3	5.9	4.6	3.4	8.0	6.2	6.5	12.8	8.6	4.6	7.8	6.8	2.5	7.8	5.8	7.1	11.9	8.6	5.1	6.1	5.7
Ho	0.7	1.2	0.9	0.6	1.6	1.3	1.3	2.4	1.7	0.9	1.6	1.4	0.4	1.6	1.2	1.3	2.2	1.6	1.1	1.3	1.2
Er	1.8	3.5	2.5	1.6	4.7	3.6	3.6	6.6	4.7	2.6	4.6	4.0	1.2	4.6	3.4	3.3	5.9	4.3	3.2	3.9	3.5
Tm	0.21	0.49	0.34	0.20	0.65	0.51	0.53	0.86	0.66	0.36	0.63	0.54	0.15	0.65	0.48	0.42	0.76	0.56	0.45	0.55	0.50
Yb	1.24	3.20	2.14	1.21	4.14	3.21	3.41	5.51	4.23	2.41	4.19	3.62	1.03	4.30	3.11	2.69	4.76	3.57	2.96	3.60	3.23
Lu	0.18	0.49	0.32	0.16	0.60	0.47	0.50	0.78	0.62	0.35	0.61	0.53	0.15	0.63	0.46	0.37	0.67	0.50	0.42	0.55	0.49
Hf	1.73	4.30	3.07	1.21	5.03	3.97	6.63	16.92	9.88	3.19	5.32	4.69	2.52	5.99	3.85	5.90	10.66	7.47	3.16	3.42	3.31
Ta	0.33	1.43	0.76	0.45	4.65	1.43	1.77	4.70	2.63	0.37	1.83	1.21	0.43	4.05	1.10	0.69	3.00	1.56	1.17	1.56	1.43
Pb	0.93	4.14	2.27	1.84	36.61	9.67	8.38	75.75	26.20	3.37	4.57	3.73	2.99	74.35	16.23	4.69	32.34	8.92	3.22	14.72	7.20
Bi	0.01	0.04	0.02	0.01	0.10	0.04	0.02	1.01	0.32	0.01	0.05	0.02	0.01	0.56	0.11	0.01	0.23	0.04	0.02	0.07	0.05
Th	0.91	2.74	1.83	0.08	7.06	1.96	7.60	11.74	10.03	1.60	2.89	2.39	1.50	8.57	4.14	3.46	6.12	4.00	1.37	1.52	1.48

(Continued on following page)

TABLE 2 | (*Continued*) Minimum, maximum, and mean (**x**) values for elemental concentrations measured for each locality in the PELIP, excluding Cr_2O_3, BaO, Te, and W. "-" not measured. * - summary stats use all sample data, including duplicates, (A) and (B) splits, and samples excluded from later MLA models for reasons discussed in *Machine Learning Workflow*.

	Etendeka (*n* = 12)*			Rio grande rise (*n* = 15)*			SG silicic (*n* = 7)*			SG Type 1 (C-N) (*n* = 34)*			SG Type 1 (S) (*n* = 52)*			SG Type 4 (*n* = 25)*			Walvis ridge (*n* = 9)*		
U	0.29	0.73	0.40	0.16	1.63	0.53	1.77	4.36	3.22	0.24	0.74	0.52	0.37	2.24	1.00	0.74	1.51	0.89	0.26	0.51	0.40
Ppb																					
Os	0.03	0.47	0.12	0.03	0.45	0.18	–	–	–	0.02	–	–	0.03	1.12	0.29	0.24	0.44	0.37	0.06	0.45	0.25
Ir	0.03	0.4	0.12	0.10	0.54	0.23	0.02	0.03	0.03	0.02	0.29	0.09	0.04	1.17	0.28	0.02	0.50	0.10	0.09	0.47	0.29
Ru	0.12	1.26	0.53	0.50	4.22	1.98	0.10	0.15	0.13	0.12	0.66	0.27	0.16	12.99	2.56	0.08	2.84	0.55	0.28	5.91	2.29
Rh	0.04	0.32	0.14	0.10	2.28	0.87	0.05	0.15	0.10	0.18	0.97	0.53	0.16	5.72	1.11	0.05	1.91	0.38	0.35	2.4	1.19
Pt	2.44	12.9	5.57	2.20	18.9	7.66	1.30	4.51	2.90	3.40	30.53	10.47	0.74	38.06	7.89	0.59	8.37	3.43	1.23	7.51	3.42
Pd	0.42	7.07	1.63	0.60	11	4.04	1.78	3.96	2.87	5.49	30.49	16.17	0.51	13.84	4.83	1.24	5.35	2.30	1.02	4.59	2.31
Au	1.12	4.9	2.71	1.00	3.92	2.25	2.43	3.81	3.12	1.85	19.25	6.46	0.18	9.09	2.42	0.37	7.60	2.45	0.08	3.57	1.05

RESULTS

Major and Trace Element Geochemistry

Table 2 gives minimum, maximum and mean measured values for all elements included in the MLA workflow. The full processed geochemical data set is available in **Supplementary Material A3**.

A selection of important anhydrous major element plots are shown in **Figure 3**, including an alkali-Fe_2O_3-MgO (AFM) ternary diagram (**Figure 3A**) and Harker plots with mineral fractionation vectors (**Figures 3B–D**); further Harker and classic normalised multi-element plots McDonough and Sun (1995) and are provided in **Supplementary Figures C1–C3** for reference. **Supplementary Figure C4** provides alteration plots for our samples, indicating low degrees of alteration throughout the set and establishing all geochemistry herein as primary signatures (Mathieu, 2018). In **Figure 3A**, Etendeka and Walvis Ridge samples represent the least evolved samples (i.e., high MgO and low SiO_2), followed by Rio Grande Rise and Serra Geral mafic samples, which are plotted tightly in the tholeiitic peak on the AFM triangle. Silicic lavas and a single mafic lava plot in the most fractionated sector. Serra Geral lavas, classified according to Licht (2018), have MgO concentrations consistently <7 wt.% while samples from Etendeka range from 5 to 15 wt.%. Rio Grande Rise lavas are subdivided into a majority ~5 wt.% (similar to Serra Geral) and Walvis Ridge samples are clustered at 7–8 wt.% MgO. All Serra Geral samples form a positive linear array in the MgO-CaO plot in **Figure 3B**, while the other localities have more subtle trends, with a mean CaO of ~10 wt.% (**Figure 3B**). Concentrations of TiO_2 groups Serra Geral lavas effectively as seen in **Figure 3C** – one group at >3 wt.% (Type 4), one at 2–2.5 wt.% (Type 1 Central-Northern), and one at <2 wt.% (Type 1 Southern and Silicic). Etendeka, Rio Grande Rise, and Walvis Ridge have generally <2.5 wt.% TiO_2. In **Figure 3D**, samples show a similar MgO-Al_2O_3 spread to MgO-CaO, with Serra Geral lavas forming a roughly positive array with Walvis Ridge samples, and the other localities a more diffuse and slightly negative trend. An inflection in the dominant trend direction is observed in all three bivariate plots at 6–7 wt.% MgO.

High-Dimensional Geochemistry Using all Variables

Principal Component Analysis

Dimensionality-reduction via PCA was performed using the concentrations of the full suite of 51 elements measured for 116 samples in the PELIP data set; the method standardises concentrations using z-scores within the script (see **Supplementary Material B**). In this variable set-up, PC1 to PC8 account for 89.06% of all data set variability (**Figure 4A**); information in higher-order PCs (i.e., PC9 and upwards above the ~90% mark in **Figure 4A**) have a minimal overall contribution to variability, hence the focus on the more significant PC1-8. A summary of PCA cumulative

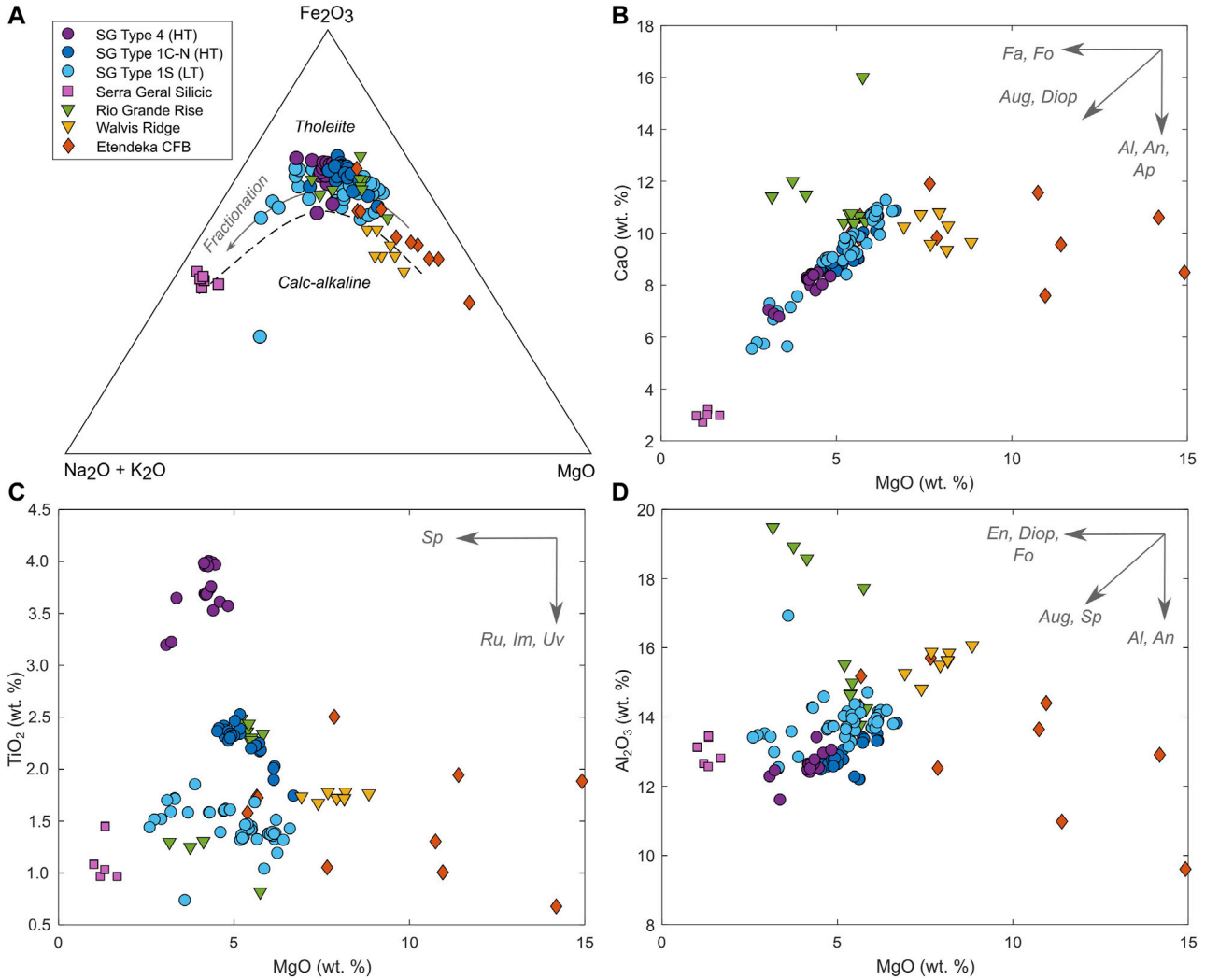

FIGURE 3 | Ternary and bivariate geochemical plots for major elements in the PELIP data set, classified by locality. **(A)** AFM (alkali-Fe-Mg) ternary plot; **(B)** MgO vs. CaO; **(C)** MgO vs. TiO2; **(D)** MgO vs. Al2O3. With fractionation vectors for evolving liquid compositions for Fo, forsterite; Fa, fayalite; Aug, augite; En, enstatite; Diop, diopside; an, anorthite; Al, albite; Sp, spinel; Uv, ulvospinel; Mg, magnetite; Ru, rutile; and Im, ilmenite.

variability and eigenvalues is provided in **Figure 4A**, showing PC1-2 alone accounting for 56% of data set variability.

Across the biplots in **Figures 4B–E**, data point and eigenvector interactions indicate how strongly a sample or element varies throughout the data set as a whole, respectively. Given the high number of variables, eigenvectors with strong similarities in direction and length are grouped together to reduce redundancy; original biplots are displayed in **Supplementary Material A3**. Although all elements were resolved individually during the PCA process, we present eigenvectors with similar lengths and directions as groups for visual clarity in **Figures 4B–E**. Overall, PC7-8 relationships (**Figure 4E**) do not depict strong or consistent trends compared to the other PC biplots described below, working west to east across the PELIP. Sample numbers reflect the 116 data lines carried through to PCA, t-SNE and *k*-means (*Machine Learning Workflow*; **Supplementary Material A3**), not those given for sample gathering or geochemical statistics in **Table 1** or **Table 2**.

- Serra Geral Type 4 (n = 19) variability is governed by: TiO_2, P_2O_5, K_2O, Rb, Zr, Hf, and light rare-earth elements (LREE) in PC1-2; MgO, Fe_2O_3, Co, V, Sc, Mn, Ni, and LREE in PC3-4; and TiO_2, LREE, Eu, Sr, Nd, Sm, and As in PC5-6.
- Serra Geral Type 1 (Central-Northern) (n = 30) variability is governed by: Fe_2O_3, Sc, V, Cu, Pd, and Au in PC1-2; Cr, Pd, and Au in PC3-4; and La, Ce, Ni, Co, U, Th, Pt, Pd, and Au in PC5-6.
- Serra Geral Type 1 (Southern) (n = 34) variability is governed by: SiO_2, Na_2O, CaO, Co, As, Ir, Ru, and Bi in PC1-2; K_2O, Al_2O_3, SiO_2, Rb, Ba, U, Th, As, Ir, Ru, Rh, Pb, and Bi in PC3-4; and a wide variety of elements in PC5-6.
- Serra Geral Silicic (n = 2) variability is governed by: the same elements as Serra Geral Type 4 in PC1-2; the same

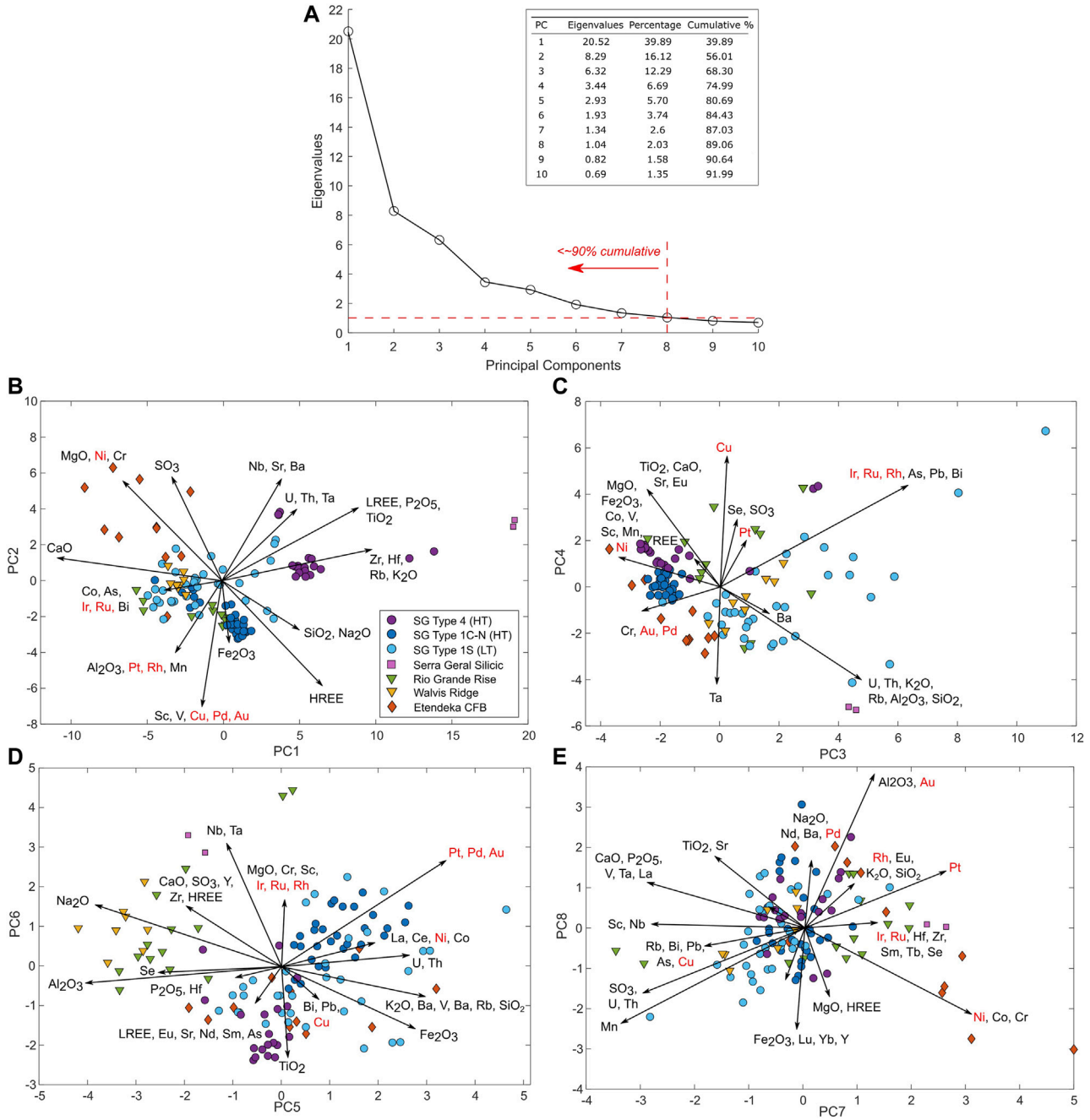

FIGURE 4 | PCA statistics and summary biplots (combined eigenvector and data point information) for 51 elements in the PELIP data set. **(A)** Eigenvalues, percentage variance and cumulative percentage variance for PC1-10, with a scree plot denoting PC8 as the highest relevant component (i.e., flat slope, cumulative percentage ~90% and eigenvalue >1.0). **(B)** Biplot for PC1 vs. PC2; **(C)** Biplot for PC3 vs. PC4; **(D)** Biplot for PC5 vs. PC6; **(E)** Biplot for PC7 vs. PC8. Data points classified by locality and eigenvectors are summarised/grouped together with similar elemental trends for ease of presentation. Red elements are of critical interest to Ni-Cu-PGE-Au studies.

elements as Serra Geral Type 1 (Southern) in PC3-4; and CaO, SO_3, Y, Zr, Nb, Ta, and heavy rare-earth elements (HREE) in PC5-6.

- Rio Grande Rise (n = 12) variability is governed by: Al_2O_3, Fe_2O_3, Co, As, Mn, Sc, V, Cu, Ir, Ru, Rh, Pt, Pd, and Au in PC1-2; TiO_2, CaO, SO_3, Se, Sr, Eu, Cu, and Pt in PC3-4; and Al_2O_3, P_2O_5, Na_2O, CaO, SO_3, Se, Y, Zr, Hf, and HREE in PC5-6.
- Walvis Ridge (n = 8) variability is governed by: CaO, Co, As, Ir, Ru, and Bi in PC1-2; the same elements as Serra Geral Type 1 (Southern) in PC3-4; and the same elements as Rio Grande Rise in PC5-6.

- Etendeka (n = 11) variability is governed by: MgO, Ni, Cr, and SO_3 in PC1-2; MgO, Fe_2O_3, Co, V, Sc, Mn, Ni, Cr, Ta, Pd and Au in PC3-4; and a wide variety of elements in PC5-6.

t-SNE

Dimensionality-reduction using t-SNE was performed using z-scores of the 51 variables. A parameter set-up of 5,000 maximum iterations (until convergence), learning rate of 200, and perplexity of 50 was selected through a heuristic approach and provided the most well-defined, evenly spaced cluster structure: **Figure 5** displays the chosen data set embedding classified by sample locality. Embeddings produced from different perplexity set-ups that were run alongside the model ultimately chosen are shown in **Supplementary D** for reference.

The t-SNE algorithm discriminates the PELIP geographical groups in **Figure 5**, with all sample types excluding the Rio Grande Rise occupying a unique sector of the embedding; the Rio Grande Rise forms three nearby sub-clusters. Serra Geral Type 4 and Silicic samples plot distinctly from the other lavas, which appear to form a continuum of multi-element compositions with smaller physical separation between each type. Etendeka and Walvis Ridge plot at the bottom of the Embedding 2. Both Serra Geral Type 1 localities occupy the centre of the embedding, with Type 1 (Southern) displaying a larger spread across the space compared to other groups. The three sub-clusters for Rio Grande Rise samples bracket Etendeka, Walvis, and Serra Geral Type 1 samples, and this appears to be a borehole control on geochemistry (i.e., **Figure 2**).

Figure 6 displays PELIP sample data arranged in the embedding space from **Figure 5**, with points coloured by z-scores for 45 of the measured major and trace elements (excluding PGE and Au), to give an account of how individual elements vary through the new embedding (as per Horrocks et al., 2019; Lindsay et al., 2021a). Elements with strong bimodal distribution (i.e., with clear, distinct zones of high and low z-scores) contribute significantly to the overall data structure, whilst those with more even or scattered z-score distributions do not. For the major elements, MgO, CaO, TiO_2, K_2O, P_2O_5, and BaO concentrations exhibit strong bimodality across the data set, whilst SiO_2, Al_2O_3, Fe_2O_3, SO_3, Na_2O, and MnO are more uniform or do not appear to have distinct variability trends apart from occasional outliers. Trace elements, Sc, V, Cr, Co, Ni, Cu, Se, Rb, Y, Zr, Hf, Th, and U exhibit bimodality of varying strength. Conversely, As, Sr, Nb, Ta, W, Pb, and Bi do not exhibit bimodal distribution. For the REE, the high z-scores progressively shift location from the top to the centre of Embedding 2 (y-axis) with increasing atomic number. This mimics a shift from Serra Geral Type 4 to Type 1 (Central-Northern) in **Figure 5**.

Figure 7 displays PELIP sample data arranged in the embedding space from **Figure 5**, with points coloured by z-scores for the PGE (excluding Os) and Au. Compared to major and trace element embedding plots, these metals are much more "nuggety," with high concentrations being much rarer than low concentrations. A small sub-cluster of Serra Geral Type 1 (Southern) samples in the far right (**Figure 5**) host very high Ir, Ru, and Rh concentrations (**Figure 7**). The highest concentrations of Pt, Pd, and Au are strongly concentrated with Serra Geral Type 1 (Central-Northern) on the left-hand side, particularly Pd and Au (again, comparing **Figures 5**, **7**). Overall, Serra Geral Type 4 and Silicic, Etendeka, Walvis Ridge, and Rio Grande Rise zones from **Figure 5** do not host high PGE concentrations, with the two Serra Geral Type 1 lavas appearing to dominate in this aspect, reflecting their statistics from **Table 2** and PGE plots in **Supplementary Figures C2, C3**.

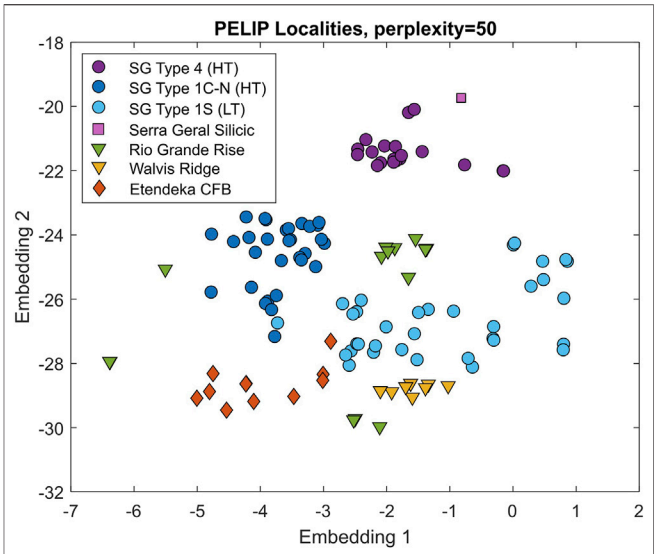

FIGURE 5 | Embedding generated using t-SNE algorithm using all 51 element z-scores. Optimum embedding was selected with a perplexity of 50 for best separability and cluster definition. Data points were classified by locality.

k-Means Clustering

Clustering using the *k*-means algorithm was performed on the i) PCs and ii) z-scores of the 51 variables for 116 samples. Models were run for *k*-values of 2–7. By comparing DBI for all model parameter set-ups, we find that the most robust model was clustering samples using PC1-8 (up to ~90% of variability; **Figure 4A**) for all variables (as suggested by Lindsay et al., 2021a), with k = 7. However on considering cluster formations, k = 7 only produces a further localised 2-point outlier cluster with otherwise identical clusters to k = 6, hence we use the k = 6 model going forward as it best describes global trends in the data set. All models from all parameter set-ups and their corresponding DBI are displayed in **Supplementary Figures E1–E3**, showing PCs to be preferential as input data.

Figure 8A displays the t-SNE layout from **Figure 5**, again classified by locality, with the same embedding classified by the *k*-means clusters from the optimal set-up displayed adjacently in **Figure 8B**. A histogram describing the subscription of new cluster classifications (Groups 1–6) in terms of their prevalence in each sample locality is given in **Figure 8C**. These six clusters define the main multi-element

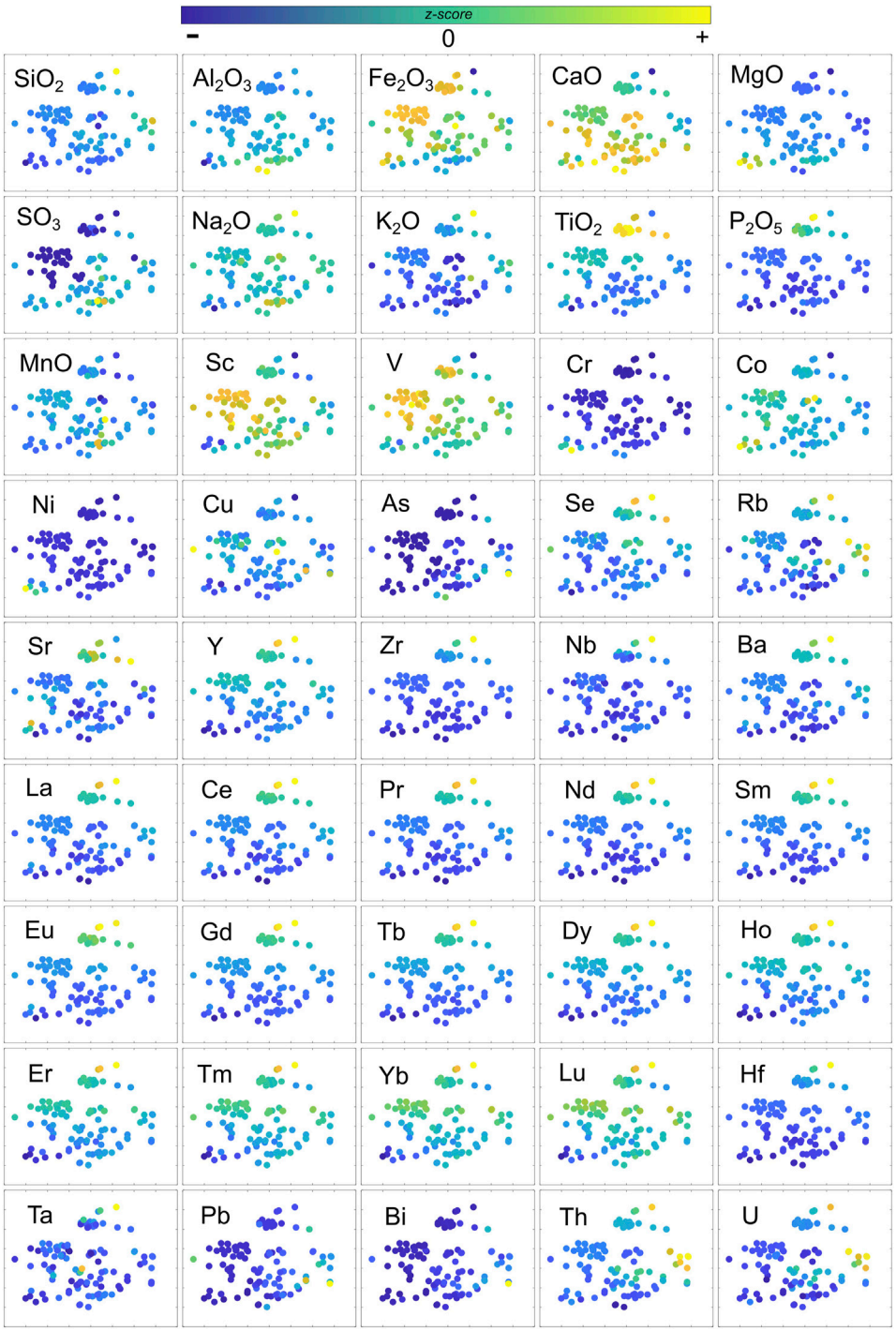

FIGURE 6 | Embedding from **Figure 5** with data points coloured by z-scores for 45 major and trace elements (excluding PGE and Au).

end-members in the lavas analysed, independent of geographic classifiers. Overall, Group 1 is exclusively found in Serra Geral Type 1 (Southern), Group 2 is exclusively found in Serra Geral Silicic, Group 4 is exclusively found in Serra Geral Type 4, and Group 6 is exclusively found in Etendeka. Group 3 appears primarily in Serra Geral Type 1 (Central-Northern) (making up the vast majority of the locality's new classification), but some Group 3 are also found in Type 1 (Southern) and Rio Grande Rise samples. Group 5 is found in all localities except Serra Geral Type 4 and Silicic, i.e., the lower half of Embedding 2 from **Figures 5**, **8B**.

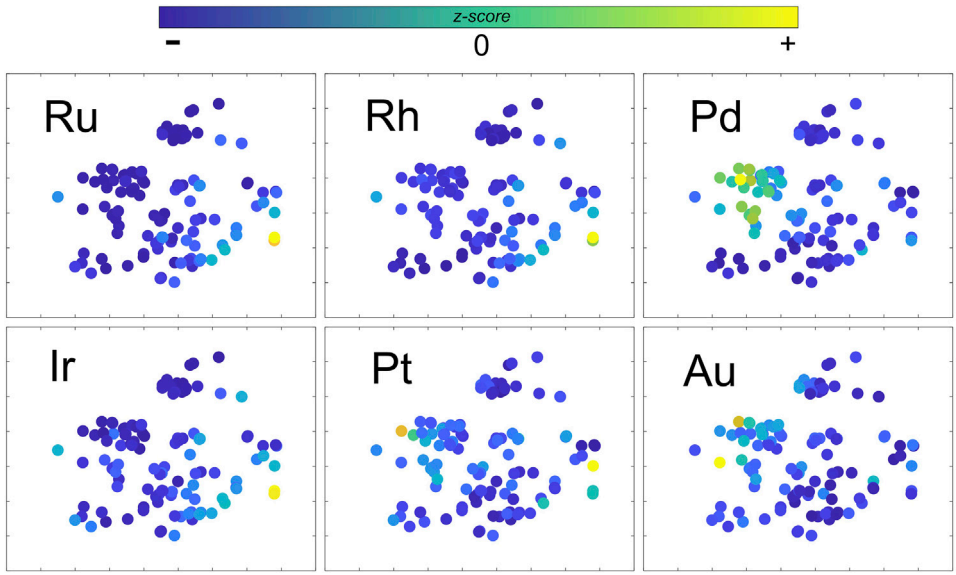

FIGURE 7 | Embedding from **Figure 5** with data points coloured by z-scores for PGE (excluding Os) and Au, arranged by atomic number.

A box-and-whisker plot detailing PGE concentrations (excluding Os due to its absence from some Serra Geral samples) per MLA-based cluster is provided in **Figure 9**. Group 1 hosts the highest mean, median, and maximum values in the data set for Ir, Ru, and Rh, and has a comparable spread of Pt concentrations to Group 3. Mean, median and maximum Pd concentrations are significantly higher in Group 3 than all other groups. Group 5 often hosts intermediate concentrations of each PGE between Groups 1 and 3. Groups 2, 4, and 6 are generally the least PGE-enriched clusters.

High-Dimensional Geochemistry Using Reduced Variables

An important application of this study is comparing results to the test study from Lindsay et al. (2021a) using the NAIP data set, both in terms of MLA workflow performance, and geochemical and geodynamic implications from their respective results. By running aspects of the MLA workflow using a reduced array of input variables, matching the eleven variables established in the NAIP data set from Lindsay et al. (2021a), we can make a substantial assessment of the relative multi-element geochemistry of the two similar plume-rift environments. In the original study, these eleven elements were measured in each NAIP locality and are synonymous with mafic-ultramafic magmas (e.g., Barnes et al., 2015). It would be inappropriate to judge interpretations of a 51-variable MLA investigation and an 11-variable MLA investigation. By running the PELIP data through the workflow a second time with the same 11 variables used in the NAIP, we can more accurately compare and contrast geochemical variability in the two settings.

Accordingly, we re-run PCA and t-SNE for the PELIP data set using *only* MgO, Fe_2O_3, TiO_2, Ni, Cu, Cr, Ir, Ru, Rh, Pt, and Pd as variables (as the eleven elements included in the NAIP study). In this reduced variable set-up, PC1-6 account for 93.10% of cumulative variability (**Figure 10A**) and PC7-11 are disregarded.

Across the biplots in **Figures 10B–D**, localities are governed by the nearby loading scores and the elements tied to them:

- Serra Geral Type 4 variability is governed by TiO_2 in PC1-2; TiO_2, Ir, Ru, and Rh in PC3-4; and TiO_2, Ir, and Rh in PC5-6.
- Serra Geral Type 1 (Central-Northern) variability is governed by Fe_2O_3, Cu, and Pd in PC1-2; Pt and Pd in PC3-4; and MgO, Cr, Cu, and Pd in PC5-6.
- Serra Geral Type 1 (Southern) variability is governed by Ir, Ru, Rh, and Pt in PC1-2; Ir, Rh, and Ru in PC3-4; and Fe_2O_3, Ni, Ru, and Pt in PC5-6.
- Serra Geral Silicic variability is governed by no particular elements in PC1-2 or PC3-4 and TiO_2 in PC5-6.
- Rio Grande Rise variability is governed by Ir, Ru, Rh, Pt, and Cu in PC1-2; TiO_2, Ir, and Rh in PC3-4; and MgO, TiO_2, Cu, Cr, and Pd in PC5-6.
- Walvis Ridge variability is governed by MgO, Cr, Ni, and Ir in PC1-2; Ru in PC3-4; and MgO, Cr, and Pd in PC5-6.
- Etendeka variability is governed by MgO, Cr, and Ni in PC1-2; Fe_2O_3, TiO_2, MgO, Cr, Ni, and Cu in PC3-4; and Fe_2O_3 and Ni in PC5-6.

Figure 11 displays the reduced variable embedding; A) classified by locality (for reference) and B) coloured by z-scored elemental concentrations for the eleven included variables. A parameter set-up of 5,000 maximum iterations (until convergence), a learning rate of 200, and a perplexity of 50 was selected as the best embedding; extra models are

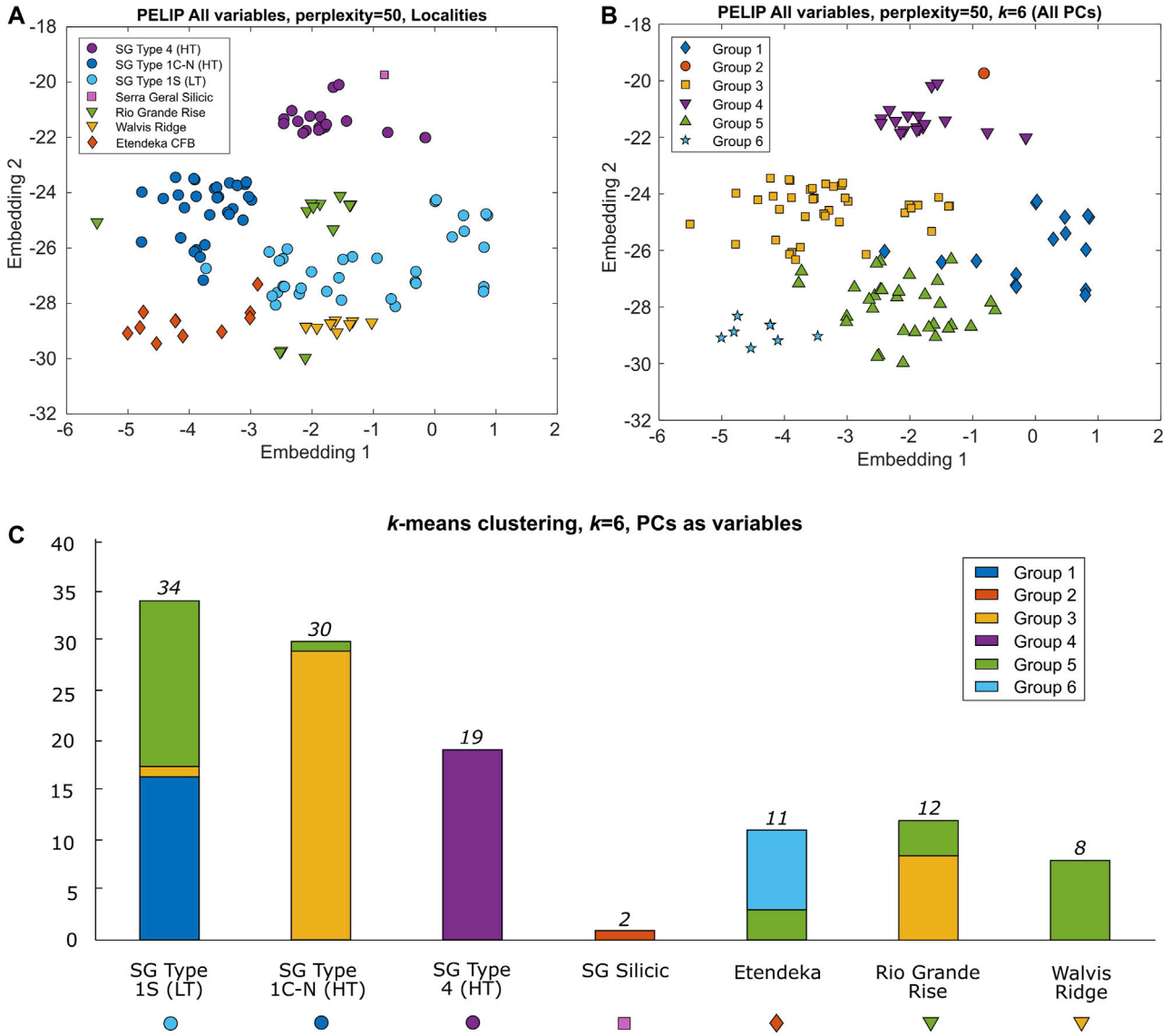

FIGURE 8 | *k*-means clustering model selection with comparison to locality classifications – **(A)** Original t-SNE embedding from **Figure 5** classified by locality (for reference); **(B)** t-SNE embedding classified by selected *k*-means clustering model (using PC1-8 from **Figure 4** as variables, $k = 6$); **(C)** Histogram comparing new cluster information from Groups 1–6 to localities.

presented in **Supplementary Figure F**. Through the new embedding space, some elements share trends – high concentrations of MgO, Ni and Cr are found in the top left, Fe_2O_3, and TiO_2 at the bottom centre; Ir, Ru, and Rh in the top right; and Pt and Pd on the right-hand side. Only Cu is distributed less clearly, although a general association with Pd is visible. Geographic sample locality zones are reasonably clear in the embedding space, with Etendeka, Serra Geral Type 4, and Silicic samples sitting separately from the rest of the localities in the central population (Serra Geral Type 1 and the ridge lavas). However, unlike the embedding using all 51 elements (i.e., **Figure 5**), individual samples often plot far from the main cluster centres, particularly for Etendeka, Walvis Ridge, and Rio Grande Rise.

DISCUSSION

MLA-Based Geochemical Interpretation

Magmatic Differentiation According to Major Elements

Figure 3 suggests that Etendeka and Walvis Ridge lavas are the most primitive in the sample suite with the highest MgO contents (**Table 2**). This is particularly notable in the AFM diagram in **Figure 3A**, in which Etendeka/Walvis samples plot earlier in the tholeiitic fractionation trend (Kuno, 1968), whilst the Serra Geral and Rio Grande Rise lavas are more evolved. Serra Geral Silicic samples are the most alkali-rich and compositionally evolved, and some Type 1 (Southern) are basaltic-andesites. The Serra Geral lavas form positive linear trends between MgO-CaO and MgO-Al_2O_3 in **Figures 3B,D**,

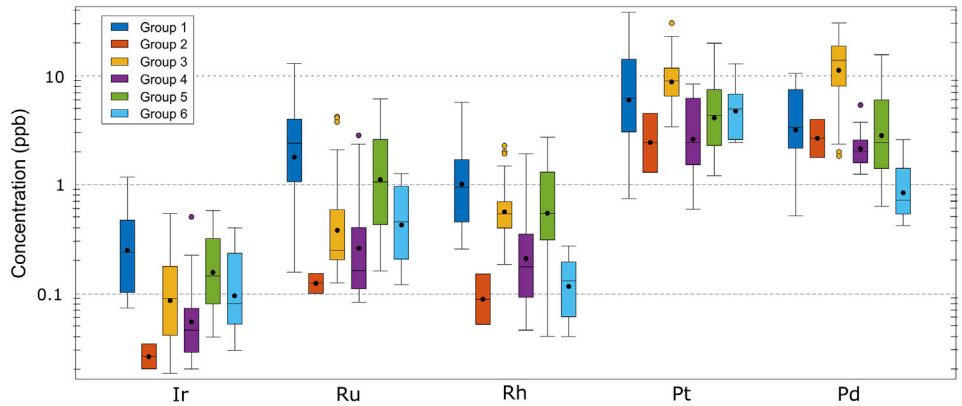

FIGURE 9 | Box-and-whisker plot for PGE (excluding Os) concentrations in the selected k-means clustering model (PC1-8 as variables, $k = 6$). Black circle – mean; horizontal line – median; box – interquartile range (Q1-Q3); whiskers – "maximum and minimum," i.e., Q1 or Q3 + 1.5 × interquartile range; coloured circles – outliers (above 1.5 × interquartile range).

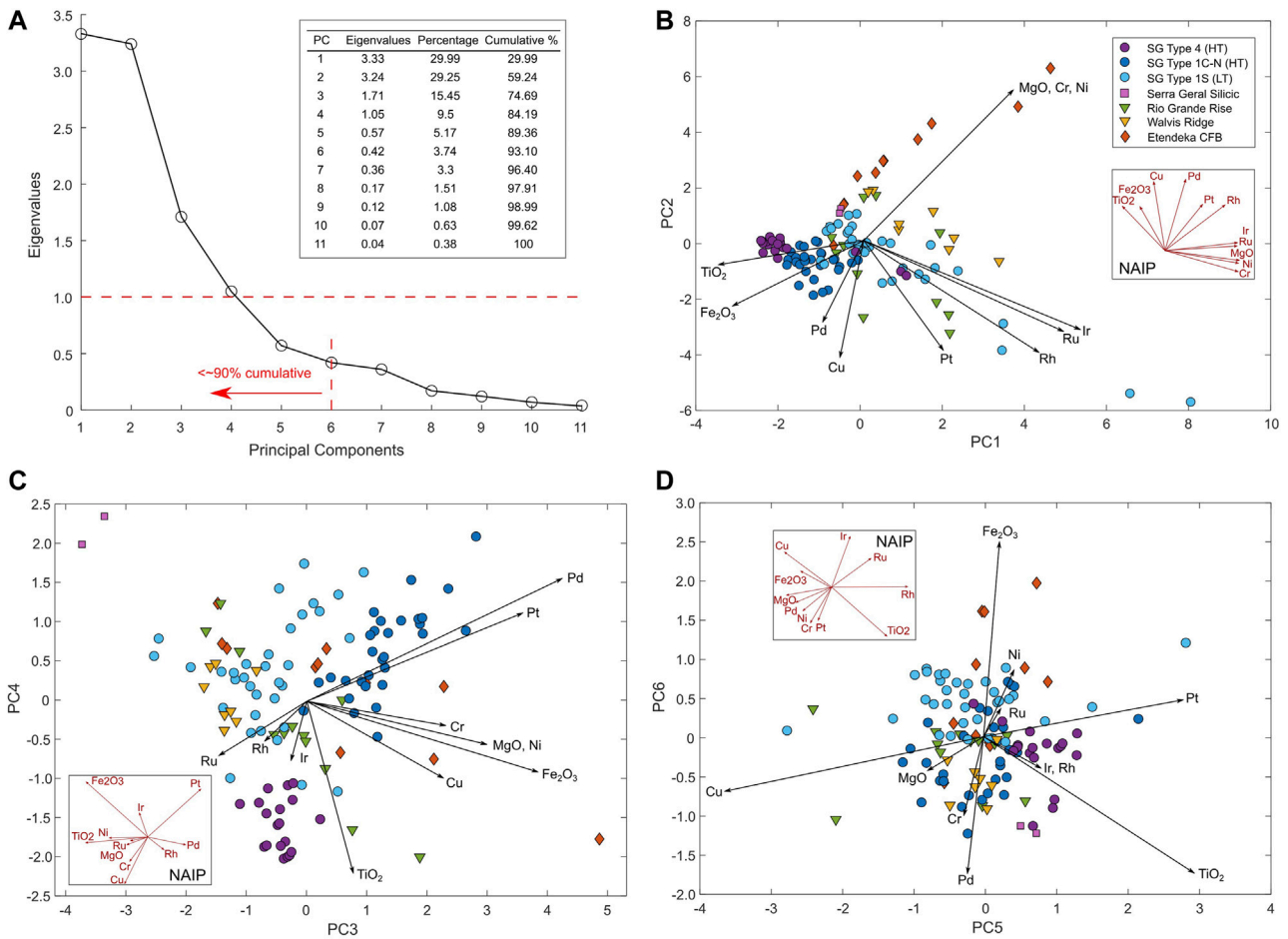

PC	Eigenvalues	Percentage	Cumulative %
1	3.33	29.99	29.99
2	3.24	29.25	59.24
3	1.71	15.45	74.69
4	1.05	9.5	84.19
5	0.57	5.17	89.36
6	0.42	3.74	93.10
7	0.36	3.3	96.40
8	0.17	1.51	97.91
9	0.12	1.08	98.99
10	0.07	0.63	99.62
11	0.04	0.38	100

FIGURE 10 | PCA statistics and summary biplots (combined eigenvector and data point information) for 11 elements in the reduced PELIP data set. **(A)** Eigenvalues, percentage variance, and cumulative percentage variance for PC1-11, with a scree plot denoting PC6 as the highest relevant component (i.e., flat slope and cumulative percentage ~90%). **(B)** Biplot for PC1 vs. PC2; **(C)** Biplot for PC3 vs. PC4; **(D)** Biplot for PC5 vs. PC6. Data points classified by locality and eigenvectors are summarised/grouped together with similar elemental trends for ease of presentation where appropriate. NAIP eigenvectors for equivalent plots in red sub-plots, from Lindsay et al. (2021a).

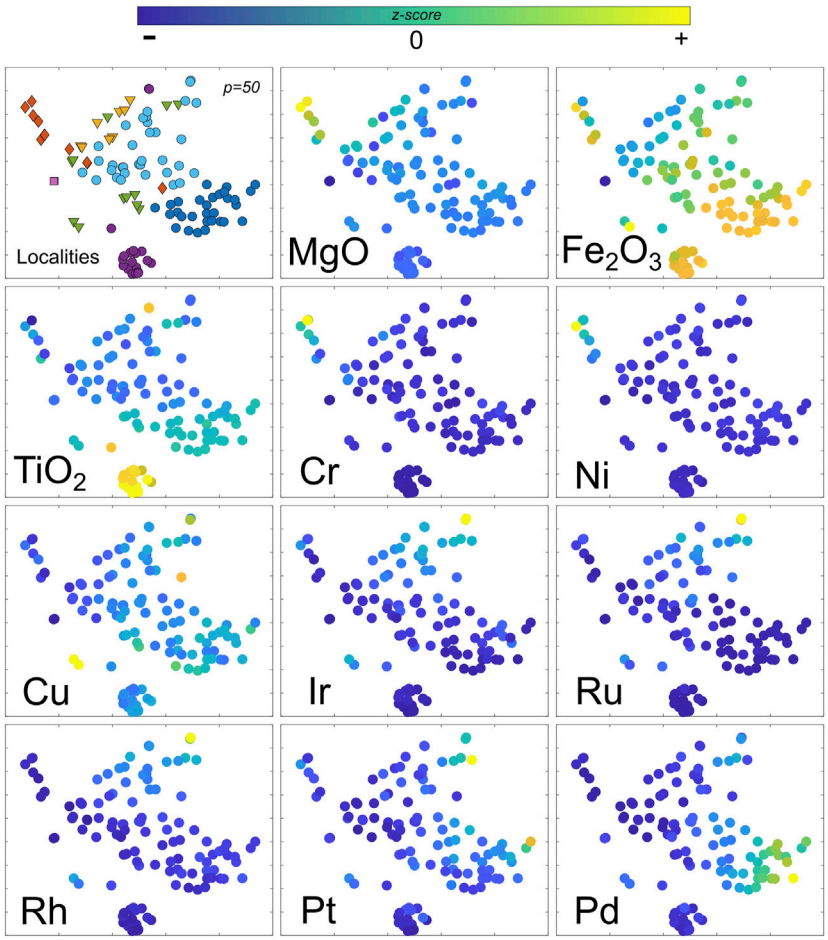

FIGURE 11 | Embedding generated for the reduced PELIP data set (11 variables), coloured by z-scores for all elements used in the model. The embedding is also classified by sample locality in the top left for reference; the key is the same used in all other plots for localities (e.g., **Figures 3**–**5**, **8**, **10**).

indicating fractionation of minerals containing these elements from the parent magma, like olivine, pyroxene, plagioclase, and/or spinel-group minerals (in agreement with Peate, 1997). Mineral fractionation vectors (e.g., Richter and Moore, 1966; Cox et al., 1979, Rollinson, 1993 and references therein) in **Figures 3B–D** and **Supplementary Figure C1** indicate stronger removal of olivine in Rio Grande Rise, Walvis Ridge, and Etendeka parent magmas compared to Serra Geral magmas. Serra Geral samples trend more closely with pyroxene and plagioclase removal (i.e., more advanced fractionation). This corroborates with Serra Geral positioning further along the AFM fractionation vector in **Figure 3A**.

Reconciling PELIP Localities With MLA-Defined Groupings

Table 3 summarises the major and trace element associations captured by the six MLA-based clusters by comparing their positions in **Figure 8B** with **Figures 6**, **7**. These classifications reinforce and allow us to succinctly describe multi-element signatures (i.e., geochemical end-members) that pervade through PCA (**Figure 4**) and t-SNE (**Figures 5**–**7**) interpretations for PELIP samples. We interpret the enrichment (or lack thereof) exhibited by each locality, working from west to east, herein.

Serra Geral Type 4 samples are defined exclusively by the Group 4 end-member in **Figure 8C** and **Table 3**. They are the highest-Ti mafic lavas, show an expectedly strong affinity for TiO_2 eigenvectors in **Figure 4** A-D, and show high-TiO_2 regions in the embedding space in **Figures 5**, **6**. This end-member also features enrichment in incompatible elements like Zr, Hf, Rb, and LREE. High-Ti Paraná basalts are typically interpreted to be from a more enriched mantle source in the literature, often connected to OIB Tristan plume signatures more than lower-Ti South American CFBs (e.g., Peate, 1997; Rämö et al., 2016; Weit et al., 2017; Beccaluva et al., 2020; Zhou et al., 2020).

Serra Geral Silicic samples are defined by the Group 2 end member (**Figure 8C**; **Table 3**), those enriched in SiO_2, alkalis, and, like Type 4, incompatible elements, such as Zr and Rb (reflected in **Figures 4**–**6**). Silicic magmas likely evolved and differentiated in the crust over time to generate their more

TABLE 3 | Summary of the defining multi-element associations in each of the six clusters generated for the data set by the k-means MLA, including precious metal contents and localities displaying these end-members, cross-referenced with **Figures 4**–**9**. SG, Serra Geral; C-N, Central-Northern; S, Southern; RGR, Rio Grande Rise; WR, Walvis Ridge; ET, Etendeka.

k-means cluster	Major/Trace associations	Metals of interest	Localities
Group 1	U, Th, As, Pb, Bi	Ir, Ru, Rh, Pt	SG 1(S)
Group 2	SiO_2, Na_2O, K_2O, Se, Y, Zr, Nb, Ba	—	SG Silicic
Group 3	Fe_2O_3, Sc, V	Pt, Pd, Au, Cu	SG (C-N), 1(S) and RGR
Group 4	TiO_2, P_2O_5, K_2O, Zr, Hf, Rb, LREE	—	SG 4
Group 5	—	Moderate PGE	SG 1(S), (C-N), RGR, WR, ET
Group 6	MgO-Ni-Cr	—	ET

silica- and alkali-rich compositions (e.g., Bellieni et al., 1984; Milner et al., 1995b; Garland et al., 1995) and may have acquired incompatible elements from the crust via extensive contamination (as per Simões et al., 2019). Precious (PGE and Au) and base metals (Ni, Cu, and Co) are notably depleted in both Type 4 and Silicic samples (**Figures 6**, **7**; **Table 3**).

Both Southern and Central-Northern Serra Geral Type 1 samples occupy adjacent spaces within the centre of the embedding from **Figure 5**, which supports their more recent classification as one major magma-type (e.g., Gomes et al., 2018; Licht, 2018), despite historically being separated into Low-Ti and High-Ti groups, respectively, in prior studies (Fodor, 1987; Peate et al., 1992; Peate, 1997). However, their detailed multi-element geochemistry illustrates differences within their data structure, including a moderate difference in TiO_2 (**Figure 3C**; **Table 2**). MLA-based clustering assigned the Group 1 and Group 5 end-members in roughly equal proportions to Type 1 (Southern) (**Figure 8C**; **Table 3**), the former designation being exclusive to the locality. Group 1 occupies an embedding space defined by very high concentrations of U, Th, As, Pb, and Bi (**Figures 6**, **7**), elements all commonly concentrated in the continental crust. Of the Serra Geral mafic lavas, Type 1 (Southern) is the most crust-contaminated magma-type and acquires much of its isotopic and lithophile geochemical characteristics from mid-upper crustal differentiation processes (e.g., Peate et al., 1992; Peate and Hawkesworth, 1996; Rocha-Júnior et al., 2013; Licht, 2018; Marques et al., 2018). Group 1 also represents lavas with the highest Ir, Ru and Rh concentrations.

Serra Geral Type 1 (Central-Northern) lavas express a consistent character through the MLA workflow, associated with Fe_2O_3, Sc, V, Cu, Pd, and Au eigenvectors (**Figure 4**), and high concentrations of these elements in the far left of the t-SNE plots (on comparing **Figures 6**, **8B**). The Group 3 end-member, found primarily in Type 1 (Central-Northern) lavas, captures the majority of the multi-element signature from this association (**Figures 8A–C**; **Table 3**). Evidently, the main difference between the two Type 1 varieties is the metal basket associated with their dominant end-members, given that their petrological definitions (**Figures 3A–D**) are reasonably consistent.

Rio Grande Rise and Walvis Ridge samples are generally less tightly defined in PCA and t-SNE spaces, but overall plot similarly to Serra Geral Type 1, appearing between clusters of Type 1 (Southern) and Type 1 (Central-Northern) in **Figure 4B** and below them as linear arrays in the embedding space (**Figure 5**). The two ridge lava types were classified primarily into Group 5 (**Figure 8C**), which is found in most localities in some amount and could thus be described as a background end-member, occupying the central embedding zone of high CaO and moderate Fe_2O_3, Na_2O, Al_2O_3, MnO, Sc, and V (i.e., z-score ≈ 0; **Figures 4B–D**, **6**, **7**, **Table 3**). This end-member is poorer in REE than other localities (especially Serra Geral Type 4 and Silicic), denoting a less enriched mantle source (i.e., shallower melts beneath a thinner lithosphere) and/or minimal crustal involvement (e.g., Le Roex et al., 1990; Gibson et al., 2005; Willbold and Stracke, 2006; Homrighausen et al., 2019). It should be noted that although the Rio Grande Rise fits within similar multi-element clusters like the Walvis Ridge, there is a degree of geochemical variability between the three IODP drillholes from which the lavas were sampled (**Figure 2**), with t-SNE and *k*-means clustering clearly segregating them in **Figures 5**, **8A-C**. Rio Grande Rise also features a significant amount of points classified as Group 3, which otherwise defines Serra Geral Type 1 (Central-Northern). However, these points plot as a separate sub-cluster of Group 3 in the centre of the embedding (**Figures 8A,B**) indicating variability between localities within the classification (**Figure 8C**).

Finally, Etendeka samples show a strong trend towards MgO, Ni and Cr eigenvectors (**Figure 4B**) and embedding sectors (**Figures 5**, **6**), a multi-element association also identified in NAIP lavas (Hughes et al., 2015; Lindsay et al., 2021a). Etendeka is the only locality to be classified in Group 6 (**Figure 8C**; **Table 3**), a multi-element end-member that likely represents high degree partial melts with predominant asthenospheric signatures (e.g., Gibson et al., 2005; Zhou et al., 2020). The literature suggests that many basalts from the Etendeka CFBs were particularly enriched in MgO due to higher temperature melting (e.g., Jennings et al., 2017; Natali et al., 2017; Jennings et al., 2019; Beccaluva et al., 2020), producing different magma compositions to the entire Paraná CFB sequence, which is less primitive in terms of MgO concentrations in comparison (**Figure 3**). The exclusivity of Group 6 to Etendeka and Groups 1–4 to Paraná and the Rio Grande Rise suggests a strong asymmetry to geochemistry on either side of the Tristan plume-rift system, explored further in the following sections.

Onshore vs. Offshore Trends in the PELIP

The clustering of localities into distinct *k*-means groups indicate that, despite all PELIP lavas being attributed to melting imposed by the temperature anomaly from the Tristan plume, mutable source components exist in the corresponding parent magmas. This may reflect the rapidly shifting geodynamic conditions in the (now) PELIP during the Creataceous period and the knock-on effect this has on melting processes. For the onshore portions, the High-/Low-Ti split is commonly thought to represent geochemical zonation in the plume (i.e., lavas produced in line with the plume head focus, and lavas that are more peripheral, respectively) (e.g., Gibson et al., 1999; Zhou et al., 2020). This led to localised heterogeneous melting processes producing distinct multi-element signatures as a net effect (as per Rämö et al., 2016). In general, Low-Ti content represents crust-contaminated magmas; High-Ti content represents less contaminated intracontinental magmas (e.g., Peate et al., 1992; Rocha-Júnior et al., 2013; Natali et al., 2017; Licht, 2018; Marques et al., 2018). However, there are many other processes affecting the final signatures including melt regime differences, mantle source composition and fractional crystallisation. All Type 1 (Southern) and Silicic onshore PELIP lavas exhibit geochemical evidence for crustal contamination, such as elevated heavy REE, Rb, U and Th, and low Nb and Ta (Pearce, 2008) (**Figure 6**). These signatures are not present in the volcanic ridge or active hotspot lavas, suggesting that the processes or mantle components creating these melts were only present during the plume head CFB phase (c. 135 to 128 Ma) (e.g., Ussami et al., 2013; Graça et al., 2019). As the plume focus moved offshore into the new ocean basin, this CFB geochemical signature was no longer generated, reinforcing the link between Low-Ti lavas and the continental lithosphere and SCLM (Thompson and Gibson, 1991; Gibson et al., 2005).

There is a well-established asymmetric distribution in isotope and trace element geochemistry across the PELIP (e.g., Piccirillo et al., 1988; Peate and Hawkesworth, 1996; Turner et al., 1996), and this together with greater preserved volumes of lava in Paraná and different sub-crustal thicknesses under both CFB regions (Gallagher and Hawkesworth, 1994) demands care in reconciling MLA-based interpretations with geodynamic processes. Despite a common regional rifting event in the opening of the South Atlantic, centred roughly on the Tristan plume, the multi-element geochemistry of PELIP lavas on the South American and African plates are different in terms of end-members identified using MLA (summarised in **Figure 8**) and PGE concentrations (**Figure 9**). In both Paraná and Etendeka, the High-Ti lava types are the products of partial melting of a mantle source enriched in incompatible elements and LREE (Rämö et al., 2016; Jennings et al., 2019; Zhou et al., 2020) suggest that this likely represents a deeper asthenospheric source undergoing low-degrees of partial melting under a thick lithosphere lid. Similar signatures are observed in Walvis Ridge and contemporary Tristan da Cunha lavas (Gibson et al., 2005). Most of these have distinctive high $^{87}Sr/^{86}Sr$ and low $^{143}Nd/^{144}Nd$ signatures, interpreted as the Gough mantle component indicative of on-axis plume melts (Le Roex et al., 1990; Weaver, 1991; Willbold and Stracke, 2006; Homrighausen et al., 2019; Zhou et al., 2020), similar to Enriched Mantle I (EMI) OIB signatures (e.g., Zindler and Hart, 1986). In Paraná, the Gough isotopic component is not present in Serra Geral lavas despite major and trace element similarities to OIB. This implies that although representing plume-derived melts, these magmas may be from a more passive plume melting influence compared to Etendeka (Turner et al., 1996) and must at the very least involve different mantle components to begin with. Serra Geral Type 1 varieties are even further removed from this Gough isotopic component and some studies argue that these lavas do not contain any isotopic evidence for direct plume involvement. Paraná and Etendeka CFBs could consequently represent geochemical end-members of SCLM and asthenospheric material in intracontinental magmas, respectively (e.g., Stroncik et al., 2017; Beccaluva et al., 2020).

Precious Metals

PGE Variations Throughout the PELIP

Throughout the PELIP, the concentrations and multi-element signatures of PGE and Au are distinctive in each locality (**Figure 9**; **Tables 2, 3**). In PCA biplots (**Figures 4B–E**) and embeddings (**Figure 7**), eigenvectors and/or high-concentrations for individual PGE and Au generally pair with each other, described herein. The MLA-based multi-element end-members defined by precious metal concentrations in *Reconciling PELIP Localities With MLA-Defined Groupings* are: Group 1 (high Ir, Ru, Rh, and Pt), found in Serra Geral Type 1 (Southern); Group 3 (high Pt, Pd, Au, and Cu), found in Serra Geral Type 1 (Central-Northern); and, to a lesser extent, Group 5 (moderate concentrations of Ir, Ru, Rh, Pt, and Pd) found throughout the PELIP. This is further illustrated by the box-and-whisker plots in **Figure 9** and classic PGE plots from **Supplementary C2-3**. Groups 2, 4, and 6 have the lowest mean and minimum concentrations of Ir, Ru, Rh, and Pd and comparable Pt concentrations to Group 5. They therefore represent geochemical end-members defined by PGE depletion, further to their major/trace element patterns in **Table 3**.

The balance between Ir-group PGE (IPGE: Os, Ir, Ru) and Pd-group PGE (PPGE: Rh, Pt, Pd) in a mafic rock generally reveals melting and mineralogical information about the parental magma (e.g., Barnes et al., 1985). We have established that Serra Geral Type 1 (Southern) lavas are enriched in IPGE and Rh (i.e., a Group 1 signature). These metals are much more compatible during melting and require higher degrees of partial melting in order to be extracted from host phases (typically PGE alloys and platinum-group minerals; PGM) into a silicate magma (e.g., Barnes and Picard, 1993; Rehkämper et al., 1997; Alard et al., 2000; Helmy and Bragagni, 2017). PPGE (especially Pd) are more incompatible, so can be assimilated

into melts from mantle phases at lower degrees of partial melting and at lower temperatures than IPGE (e.g., Holzheid et al., 2000; Maier et al., 2003; Bockrath et al., 2004; Righter et al., 2008). The Group 1 link to As and Bi variability (**Table 3**) emphasises the segregation of Ir, Ru, and Rh from the other PGE, given that phase relations have been established between Te-As-Bi-Sb-Sn (the TABS series) and Os-Ir-Ru-Rh in pyrrhotite in the orthomagmatic sulphide systems (Mansur and Barnes, 2020). Modelling from Lindsay et al. (2021b) revealed the increase in partial melting in the mantle below the thinnest section of pre-Atlantic Brazilian lithosphere facilitated melting of not only IPGE-bearing sulphides and PGM/TABS phases in the SCLM, but spinel-group minerals in which IPGE have high partition coefficients (e.g., Capobianco and Drake, 1990; Barnes and Picard, 1993; Peach et al., 1994; Pitcher et al., 2009; Park et al., 2017).

The Group 3 association of Pd, Au, and Cu found in Serra Geral Type 1 (Central-Northern) lavas could be indicative of a metasomatically-enriched mantle source. Studies suggest that the SCLM and upper asthenosphere are enriched by fluids and partial melts released from down-going oceanic crust at subduction zones, effectively re-fertilising a region of the sub-continent (e.g., Mitchell and Keays, 1981; Borisov et al., 1994; Righter et al., 2008). The metals typically associated with this process include Pd, Au, and Cu, some of the least compatible precious and base metals, which would preferentially be exsolved from a dehydrating slab (e.g., Woodland et al., 2002; Lorand et al., 2013; Tassara et al., 2017; Rielli et al., 2018; Wade et al., 2019). This process leads to the formation of base metal sulphides and accessory minerals (enriched in Pd, Au and Cu) within metasomatised SCLM. Magmas generated below this SCLM can melt these metasomatic mineral phases, incorporating their metal budget; this mechanism has been highlighted in many cratonic settings including Brazil (e.g., Zhang et al., 2008; Maier and Groves, 2011; Rocha-Júnior et al., 2013; Holwell et al., 2019; Choi et al., 2020). Data from PELIP CFBs indicates degrees of partial melting around 22.5% during plume head magmatism under a thinning lithosphere (Gibson et al., 2005), suitable for exhausting sulphides in melting sources. The presence of a metasomatic component in the melting SCLM has been identified as a key driver in the near-surface precious metal content of intraplate magmas (e.g., Powell and O'Reilly, 2007; Tassara et al., 2017). A shallower melting imposed by the thinning Brazilian landmass may have allowed for higher degrees of partial melting of the SCLM and thus elevated Pd, Au, and Cu in Serra Geral Type 1 (Central-Northern), in accordance with (e.g., Rämö et al., 2016). The link to Sc and V variability (**Table 3**) may further suggest significant metasomatic activity in rocks bearing a Group 3 signature, given the sensitivity of these elements to fluid interaction and redox conditions in the mantle (e.g., Chassé et al., 2018; Woodland et al., 2018 and references therein).

The more comparable Pt concentration levels through all localities (**Figure 7**; **Table 2**) and *k*-means clusters (**Figure 9**) is likely a representation of an absence in Pt anomalies. This may indicate that there are no Pt-enriched domains within the melting environment and therefore no increased abundance in Pt-bearing PGM. Whereas Os, Ir, Ru Rh, and Pd (plus Au) each tend to form more element-specific mineralisation phases (Lorand et al., 2008 and references therein), Pt can be found in a wider range of hosts (i.e., Mss, Cu-sulphides, and Pt-alloys) largely on account of its complex partitioning behaviour under upper mantle conditions (Lorand and Alard, 2001). Therefore, low levels of Pt could be introduced to the magma from a wide variety of locations, contrasting with the spiked Ir-Ru-Rh and Pd-Au-Cu signatures from SCLM-derived Type 1 melts.

The fact that other localities in the PELIP do not have significant PGE enrichments further reinforces the ideas of Gibson et al. (2005), Rämö et al. (2016), and Beccaluva et al. (2020) that suggest variable melting processes under Paraná and the rest of the PELIP in response to lithospheric thinning drive variable incorporation of SCLM metals. The PGE signatures are unlikely to be inherited from the plume, otherwise, they would be ubiquitous in melts in the region, especially in the Rio Grande Rise and Walvis Ridge, which are distal to the SCLM. Modelling from Lindsay et al. (2021b) directly attributed PGE enrichment in Serra Geral Type 1 lavas to enhanced degrees of partial melting exhausting SCLM sulphides and spinel. It should be noted that Rio Grande Rise samples were mainly clustered into Group 3 (**Figures 8A–C**), the end-member otherwise typifying Serra Geral Type 1 (Central-Northern) lavas and their distinctive enrichment in Pd, Au, and Cu. The Rio Grande Rise samples occupy a small population of Group 3 points in the very centre of the embedding space (**Figure 5**), where Pt, Pd, Au, and Cu concentrations are moderate to low (**Figure 7**). As such, whilst the majority of Rio Grande Rise lava major and trace element concentrations are similar enough to Type 1 (Central-Northern) to merit their classification in a single end-member cluster, the high Pd-Au-Cu association is unique to the continental lavas alone. This is an important feature in the argument for SCLM involvement in metallogenesis, as whilst we have magmas generated to feature similar multi-element signatures, the connection to the Brazilian and African cratons must drive the individual precious metal deviations expressed. This may also potentially reflect different metal inheritance or "pre-conditioning" on either side of the (current) Atlantic, as described by Lindsay et al. (2021b) for the Brazilian craton and by Hughes et al. (2015) across the North Atlantic craton and NAIP.

Implications for Geodynamics and Metallogenesis

With a focus on PGE, Cu, and Au, it is evident that specific stages in PELIP development are prone to higher metal concentrations than others. The Serra Geral Type 1 (Southern) and Type 1 (Central-Northern) samples, in particular, are the major hosts for elevated PGE contents through the region; Ir-Ru-Rh-Pt for the Southern magma-type and Pt-Pd-Cu-Au for the Central-Northern magma-type. In terms of processes controlling these differences, by combining information from all aspects of the MLA workflow and data from associated literature, we can suggest a working model for metallogenesis in the PELIP,

centred around the temporal changes to regional multi-element geochemistry and PGE concentrations in this new data set.

There have been three geochemical/geodynamic developmental stages in the PELIP: 1) continental lavas in Paraná and Etendeka, featuring the zoned plume head and High/Low-Ti bimodality; 2) Rio Grande Rise and Walvis Ridge plume tail hotspot trails, featuring the absence of crustal contaminated components; and 3) separated Tristan and Gough trails representing two "flavours" of concurrent mantle plume magma and the cessation of South American plate volcanism (**Figures 2A,B**). The relative timing of eruptive sequences in Paraná is complicated given the high flux rates (Bellieni et al., 1984; Thiede and Vasconcelos, 2010; Licht, 2018; Rossetti et al., 2018), but overall, Type 4 progresses stratigraphically in most sequences to Type 1 (Central-Northern) in the north-west, whilst Type 1 (Southern) and Silicic lavas erupted in the south-east of the basin. Their geochemical characteristics (**Figures 3A–D**, **4B–E**, **5**) and the cluster designation of each magma type (**Figure 8C**) are distinct enough to be considered as four individual but synchronous geochemical processes between 135 and 134 Ma. Etendeka lavas erupted at a similar time to Type 1 (Southern) at around 134 Ma, and Rio Grande Rise and Walvis Ridge lavas erupted once the rifting had progressed to an oceanic setting from 128 Ma until the Tristan-Gough bifurcation at ~70 Ma (**Figures 1A,B**). The overall transition from thick to thin continental lithosphere and finally to oceanic lithosphere is the control on all magma geochemical variability from a single plume source, and we suggest that the PGE distribution varies as a function of this.

The High-Ti lavas of Paraná were generated by small degrees of melting as the plume head decompressed beneath the thickest part of the Brazilian lithosphere, and despite being enriched in REE elements as per Enriched Mantle 1 (EM-1) OIB geochemistry, this melting regime (deeper asthenosphere, low degree partial melting) did not allow PGE acquisition on Type 4 magma ascent (Rämö et al., 2016). Geographically closer to the rift-zone, and on the axial sections of the plume head, Type 1 magmas were generated at shallower asthenospheric/SCLM depths, and higher degrees of partial melting (Beccaluva et al., 2020), which allowed for the melting and integration of SCLM PGE-bearing sulphides into magmas. Isotopic signatures from such melts can often be matched to cratonic xenolith compositions representative of the local SCLM (e.g., Gibson et al., 2005 and references therein). Type 1 (Central-Northern), from a slightly thicker lithosphere, exceeded melting conditions for PPGE sulphides (including Au and Cu). Type 1 (Southern), adjacent to the incipient ocean opening and thus under a thinner lithosphere, incorporated even shallower and higher degree partial melts and IPGE-bearing sulphides and/or spinel-group minerals to boost their concentrations in line with the Group 1 end-member (Lindsay et al., 2021b). On the African plate, Etendeka parent magmas were extracted under similar plume and asthenospheric conditions, but evidence suggests that (similar to Serra Geral Type 4 magmas) the involvement of deeper, hotter, and more plume-derived melts in their genesis (e.g., Marsh et al., 2001; Rämö et al., 2016; Jennings et al., 2019) did not facilitate incorporation of PGE from the shallower SCLM. An alternative explanation could be simply that SCLM components involved in Type 4 and Etendeka melts were not significantly pre-enriched, leading the resulting net multi-element geochemistry to be dominated by the asthenospheric components. From their similar chalcophile concentrations, the sulphur saturation histories of each region appear broadly equivalent (i.e., **Supplementary Figure C1**), so it is unlikely that this process differentiated the precious metal signatures.

Rio Grande Rise and Walvis Ridge lavas feature the background/non-enriched signatures also common in the Type 1 lavas (i.e., Groups 2 and 5; **Figure 8**), with the lack of PGE-rich end-members reflecting the absence of SCLM input in offshore melting (e.g., Gibson et al., 1999; Hoernle et al., 2015; Zhou et al., 2020). Whilst early oceanic PELIP lavas show isotopic evidence for a small component of SCLM present in melts (e.g., high $(La/Nb)_n$, low εNd and $^{206}Pb/^{204}Pb$), this has been attributed to contamination by delaminated cratonic slivers from continental break-up in the sub-oceanic melt column (Douglass et al., 1999; Le Roux et al., 2002; Gibson et al., 2005). More recent enriched oceanic ridge lavas with isotopic compositons, unlike Brazilian or African SCLM components (high $^{206}Pb/^{204}Pb$ and $^{87}Sr/^{86}Sr$; Gibson et al., 2005), have instead been linked to a deep mantle source and are thus more akin to classic EM-1 signatures (e.g., Wilson, 1992). The incorporation of SCLM remnants in westernmost Rio Grande Rise magmas are potentially reflected in their multi-element resemblance to onshore Type 1 lavas in terms of *k*-means cluster distribution (i.e., the ubiquitous Group 5; **Figure 8C**), but this is restricted purely to major and trace element similarities, not precious metals.

In summary, the manner in which different melts are generated directly affects resultant magma multi-element geochemistry and, in particular, PGE concentrations, as demonstrated across the PELIP. The "sweet spot" for PGE enrichment in magmas across the region appears to be linked to late-stage Serra Geral Type 1 CFBs. This is demonstrated to be a product of the imminent separation of South America and Africa where lithospheric un-lidding promoted higher degrees of partial melting and therefore incorporation of a greater proportion of SCLM-derived metals (whether through direct partial melting of the SCLM itself and/or through contamination) (as per Lindsay et al., 2021b). The geochemical signature increasingly found in PELIP hotspot trail lavas through time denotes a more prevalent involvement of the Tristan-Gough plume component, accompanied by the waning of SCLM-derived components as the South Atlantic opened. This is similar to the observation that the metal basket of the NAIP changed spatially and temporally as the North Atlantic rifted (Hughes et al., 2015; Lindsay et al., 2021a).

Comparison With the Icelandic Plume

The extra step of recreating the input parameters from the NAIP for the new PELIP set has enabled us to directly compare

the interpretations for lavas derived from the two mantle plumes associated with the opening of the Atlantic Ocean. Broadly, the multi-element associations for major and trace elements in PCA biplots for both regions are similar – the two persistent associations are MgO-Ni-Cr and Fe_2O_3-TiO_2-Cu (**Figure 10B** and its inset NAIP arrays, and **Figures 11A,B**). However, PGE distribution differs between the regions, particularly for Ir-Ru-Rh eigenvectors in the highest-order PCs (i.e., the majority of data set variability). In the NAIP, these metals are always associated with MgO-Ni-Cr in dimensionality reduction results, with particularly high multi-element concentrations found in Greenlandic onshore lavas (Lindsay et al., 2021a). In the PELIP, Ir, Ru, and Rh variabilities are rarely associated with the MgO-Ni-Cr group eigenvector(s), even at lower-order PCs (**Figures 10B–D**). For the PELIP, the highest PGE concentrations are not associated with the two major multi-element end-members, which is logical given that the Serra Geral Type 1 hosts are neither the highest-Ti localities (like Type 4) or the highest-MgO localities (like Etendeka and the ridges). Thus, PGE variability in the PELIP decouples from the trends established in the NAIP, immediately differentiating the metallogenic characters of the two regions. We know from MLA results using all PELIP variables that PGE enrichment coincides with distinct sets of lithophile indicators, differentiating the processes that generate high Ir-Ru-Rh lavas.

In the Lindsay et al. (2021a) study, heterogeneous Pt/Pd variability throughout the NAIP reinforced prior work suggesting that the lithospheric keels around continent edges (i.e., modern day Scotland and Greenland) were variably enriched in metals added through metasomatic processes (Hughes et al., 2014 and references therein). This gives rise to notable PGE-bearing magmatic deposits on both sides of the plume-rift system in the Isle of Rum and Skaergaard Complex (e.g., Andersen et al., 1998; Pirrie et al., 2000; Power et al., 2000; Nielsen et al., 2014; O'Driscoll et al., 2014; Andersen et al., 2017). In the PELIP, at least for Pd concentrations, enrichment associated with the Group 3 end-member (**Figure 9**) appears much more consistent and focused in a single locality, Serra Geral Type 1 (Central-Northern) (**Table 2**).

Rämö et al. (2016) suggested a transition from the deeper-sourced Type 4 magmas to shallower melting depths for Type 4 generation, based upon modelling of garnet and spinel lherzolite stability zones in the asthenosphere. An increased degree of partial melting can effectively sequester more Pd-bearing metasomatic sulphides from the SCLM. Overall, Pd distribution is described more concisely by the MLA approach in the southern province compared to the north (Lindsay et al., 2021a), even with reduced variable information. No major PGE-bearing intrusions have been discovered in the Paraná Basin at the time of writing, but judging by the signatures in contemporaneous lavas, from a mineral systems perspective, intrusive bodies akin to Type 1 (Southern) or (Central-Northern) composition may prove fruitful for mineral exploration.

This study further reiterates a finding from the NAIP study: Pt is overall a sporadically distributed metal in comparison to the other PGE. Its disordered placement in embedding plots (**Figures 7**, **11**), more even enrichment in all PELIP multi-element signatures (**Figure 9**) and overall decoupling from major eigenvector associations (**Figures 4B–E, 10B–D**) illustrates this behaviour. By recognising such distribution in the PELIP, via both full and reduced data set MLA results, it supports the true "nuggety" geochemistry of Pt (*PGE Variations Throughout the PELIP*) and genuine heterogeneity of SCLM metal enrichment is persistent through different plume-rift systems.

Overall, the PELIP has a much more distinctive locality-based classification system, and MLA-based clusters generally support separate localities having unique geochemical signatures. In contrast, in the NAIP all three *k*-means clusters generated for the data set can be found in all five localities, indicating that each sample location exhibits a degree of similarity with the others and no single area has its own exclusive signature. This of course does not extend to Pt and Pd, which behave independently from all other variables in the NAIP Lindsay et al. (2021a) study. Comparing this to the PELIP, four of the six optimum *k*-means clusters generated for the full data set (51 variables) are exclusive to a single locality, a fifth is almost wholly found in Serra Geral Type 1 (Central-Northern), and the sixth is a background end member (**Figures 8B,C**; **Table 3**). Even when using $k = 3$ and the PCs of eleven variables (see **Supplementary Figures G1, G2** for selected reduced-variable clustering results), the model best-suited to the NAIP data set, PELIP localities cluster far more neatly into three groups than the NAIP (roughly correlated to Low-Ti, High-Ti, and anomalously high PGE), despite a smaller sample set. This illustrates that overall the PELIP is asymmetrical with stronger and more distinct multi-element signatures in each sample locality (i.e., end-member distribution in **Figure 8C**), whilst the NAIP is more symmetrical with more geochemical similarity in each locality.

Despite numerous differences, we can draw important similarities between the two plume-rift localities as PGE metallogenic systems. East Greenland (i.e., lava samples from the region near the Skaergaard Complex), where many of the highest multi-element PGE concentrations were found in the Lindsay et al. (2021a) study and the original investigations (Lightfoot et al., 1997; Philipp et al., 2001; Momme et al., 2002; Momme et al., 2003; Hughes et al., 2015), is the geographic equivalent of the Serra Geral Type 1 lavas in the PELIP. Both localities are west of the rift, constitute some of the youngest continental lavas, and feature notable PGE enrichments, with the specific precious and base metal basket per locality varying between the north and south. In this sense, there appears to be a continent-edge (i.e., newly rifted craton margin) control on PGE enrichment (e.g., Gibson et al., 1999; Hughes et al., 2015; Hughes et al., 2017). However, as demonstrated in this study, the PELIP does not mirror this enrichment in the east and Etendeka lavas are consistently different from all onshore Paraná lavas through all MLA results (best summarised in **Figure 8C**), particularly in PGE concentrations. In contrast, Scotland and Ireland in the NAIP

(the northern geographic equivalents of Etendeka onshore lavas) have multi-element geochemistry similar to Greenlandic lavas (Lindsay et al., 2021a) and also host PGE-bearing intrusions in the Isles of Rum, Mull, and Skye (e.g., Andersen et al., 2002).

Evidently, the subtle differences in plume-rift architecture significantly influence regional geochemistry despite contemporary lavas having erupted very close together before drifting to their current geographic position. The notable missing EM-1 isotopic component through much of the Serra Geral lavas plays a key role in PELIP heterogeneity by emphasising the more passive plume melting regime in comparison to the rest of the region. This may be a result of i) changes in mantle sources as a response to differential lithospheric un-lidding; ii) markedly different cratonic composition or structure in the melting environment; or iii) heterogeneous melting sources. The marked decrease in precious metal content as the plume progressed further from the continent in both the PELIP and NAIP serves as substantial evidence that metal baskets are inherently linked to SCLM input in transitional continent-ocean plume settings.

CONCLUSION

A widespread account of PGE concentrations across the PELIP using our geochemical MLA workflow has illustrated the importance of continent-edge geodynamic conditions in controlling the metal basket of plume-derived intraplate melts.

1) Dimensionality reduction and multi-element analyses describe distinct signatures for each of the PELIP sample localities. PGEs are focused strongly in the Serra Geral Type 1 (Southern) and Type 1 (Central-Northern) lavas in Paraná, with each having its own set of associated metals – Ir-Ru-Rh-Pt for the former, Pt-Pd-Au-Cu for the latter. These enrichments are driven by enhanced degrees of partial melting attributed to shallowing melt foci in response to lithospheric thinning between 134 and 128 Ma.
2) PGE enrichment is asymmetrical across the PELIP, as the Etendeka equivalents of the Type 1 lavas are notably un-enriched in all PGE analysed, which is attributed to the dominance of deeper, hotter but lower degree plume-derived partial melts instead of the passive melting of SCLM material under Paraná.
3) The western and eastern oceanic ridges show multi-element similarities to their onshore equivalents when considering major and trace elements, but they lack high concentrations of precious metals, which reinforces the hypothesis that PGEs are being supplied to Serra Geral Type 1 magmas by the melting of SCLM under a progressively thinning Brazilian lithosphere.
4) On comparing the Tristan plume system to the similar Icelandic plume system (from which the test of the MLA workflow was conducted), despite recognising some multi-element associations common in both regions, PGE enrichment is different in each. The Icelandic system does not feature asymmetry in PGE enrichment either side of the Atlantic Ridge. Therefore we conclude that, whilst SCLM enrichment is complex and variable in a plume-rift mineral system, there are common processes for how these metals are acquired.
5) By using unsupervised MLA, we were able to: characterise PELIP sample multi-element variability quickly, objectively, and effectively; validate our MLA-based major and trace element geochemical interpretations against the region's geodynamic history; and then overlay new PGE interpretations on top of location-specific magmatic processes.

DATA AVAILABILITY STATEMENT

The original contributions presented in the study are included in the article/**Supplementary Material**, further inquiries can be directed to the corresponding author.

AUTHOR CONTRIBUTIONS

JL undertook sample acquisition and preparation, all lab work, machine learning analyses, plotting and writing of manuscript. HH supervised project and provided substantial edits to manuscript drafts. CY helped formulate machine learning workflow via Python and provided substantial edits to manuscript drafts. JA supervised project, assisted on sample acquisition fieldwork and provided feedback on final draft edits. IM supervised PGE lab work and provided feedback on final draft edits.

FUNDING

Funding provided solely by the University of Exeter's Vice-Chancellor Scholarship for Post-Graduate Research, an internal funding programme for early career post-graduate researchers.

CONFLICT OF INTEREST

The authors declare that the research was conducted in the absence of any commercial or financial relationships that could be construed as a potential conflict of interest.

ACKNOWLEDGMENTS

The authors would like to thank Otavio Licht, Marcell Besser, and the entire Geology department of University Federal do Paraná and the Brazilian Geological Survey (CMPR) in Curitiba for their hospitality and local knowledge during the most recent sample acquisition trip to the region. We would also like to thank Edir Arioli for his field assistance on the prior trip. Thanks are extended to Bob Trumbull for supplying Etendeka lava samples to the project for which we are extremely grateful.

We would also like to thank Holger Kuhlmann and all at the IODP Repository in Bremen for helping sort, select, and ship offshore core samples, and we also thank Matthew Head for assistance using MatLab and GMT for figure preparation. Finally, we thank Gavyn Rollinson, Sharon Uren, Malcolm Spence, Steve Pendray, and Katie McFall for guidance through the various laboratory techniques used in our study. JL is sponsored by the University of Exeter's Vice-Chancellor Scholarship for Postgraduate Research.

SUPPLEMENTARY MATERIAL

The Supplementary Material for this article can be found online at: https://www.escubed.org/articles/10.3389/esss.2021.10039/full#supplementary-material

Datasheet 1 | Supplementary A.

Datasheet 2 | Supplementary B.

Datasheet 3 | Supplementary C to F.

REFERENCES

Alard O., Griffin W. L., Lorand J. P., Jackson S. E., and O'Reilly S. Y. (2000). Non-chondritic Distribution of the Highly Siderophile Elements in Mantle Sulphides. *Nature* 407, 891–894. doi:10.1038/35038049

Andersen J. C. Ø., Power M. R., and Momme P. (2002). "Platinum-Group Elements in the Palaeogene North Atlantic Igneous Province," in *The Geology, Geochemistry, Mineralogy, and mineral Beneficiation of Platinum-Group Elements*. Editor L. J. Cabri (Montreal, QC: Montréal, Québec, Can. Inst. Mining, Metall. Pet. CIM Spec.), 637–667.

Andersen J. C. O., Rasmussen H., Nielsen T. F. D., and Ronsbo J. G. (1998). The Triple Group and the Platinova Gold and Palladium Reefs in the Skaergaard Intrusion; Stratigraphic and Petrographic Relations. *Econ. Geol.* 93, 488–509. doi:10.2113/gsecongeo.93.4.488

Andersen J. C. Ø., Rollinson G. K., McDonald I., Tegner C., and Lesher C. E. (2017). Platinum-group Mineralization at the Margin of the Skaergaard Intrusion, East Greenland. *Miner Deposita* 52, 929–942. doi:10.1007/s00126-016-0707-3

Baramurali M., Silversides A., and Melkumyan A. (2019). A Comparison of T-SNE, SOM and SPADE for Identifying Material Type Domains in Geological Data. *Comput. Geosci.* 125, 78–89. doi:10.1016/j.cageo.2019.01.011

Barnes S.-J., Naldrett A. J., and Gorton M. P. (1985). The Origin of the Fractionation of Platinum-Group Elements in Terrestrial Magmas. *Chem. Geology.* 53, 303–323. doi:10.1016/0009-2541(85)90076-2

Barnes S.-J., and Picard C. P. (1993). The Behaviour of Platinum-Group Elements during Partial Melting, crystal Fractionation, and Sulphide Segregation: An Example from the Cape Smith Fold Belt, Northern Quebec. *Geochimica et Cosmochimica Acta* 57, 79–87. doi:10.1016/0016-7037(93)90470-h

Barnes S. J., Cruden A. R., Arndt N., and Saumur B. M. (2016). The mineral System Approach Applied to Magmatic Ni-Cu-PGE Sulphide Deposits. *Ore Geology. Rev.* 76, 296–316. doi:10.1016/j.oregeorev.2015.06.012

Barnes S. J., Mungall J. E., and Maier W. D. (2015). Platinum Group Elements in Mantle Melts and Mantle Samples. *Lithos* 232, 395–417. doi:10.1016/j.lithos.2015.07.007

Beccaluva L., Bianchini G., Natali C., and Siena F. (2020). Plume-related Paranà-Etendeka Igneous Province: An Evolution from Plateau to continental Rifting and Breakup. *Lithos* 362-363, 105484. doi:10.1016/j.lithos.2020.105484

Begg G. C., Hronsky J. A. M., Arndt N. T., Griffin W. L., O'Reilly S. Y., and Hayward N. (2010). Lithospheric, Cratonic, and Geodynamic Setting of Ni-Cu-PGE Sulfide Deposits. *Econ. Geology.* 105 (6), 1057–1070. doi:10.2113/econgeo.105.6.1057

Bellieni G., Comin-Chiaramonti P., Marques L., Melfi A. J., Piccirillo E., and Nardy A. J. (1984). High- and Low-TiO2 Flood Basalts from the Paraná Plateau (Brasil): Petrology and Geochemical Aspects Bearing on Thier Mantle Origin. *Neues Jahrb. für Mineral.* 150, 273–306. doi:10.1093/petrology/25.3.579

Bierlein F. P., Groves D. I., and Cawood P. A. (2009). Metallogeny of Accretionary Orogens - the Connection between Lithospheric Processes and Metal Endowment. *Ore Geology. Rev.* 36, 282–292. doi:10.1016/j.oregeorev.2009.04.002

Bockrath C., Ballhaus C., and Holzheid A. (2004). Fractionation of the Platinum-Group Elements during Mantle Melting. *Science* 305, 1951–1953. doi:10.1126/science.1100160

Borisov A., Palme H., and Spettel B. (1994). Solubility of Palladium in Silicate Melts: Implications for Core Formation in the Earth. *Geochimica et Cosmochimica Acta* 58, 705–716. doi:10.1016/0016-7037(94)90500-2

Buccianti A., and Grunsky E. (2014). Compositional Data Analysis in Geochemistry: Are We Sure to See what Really Occurs during Natural Processes? *J. Geochemical Exploration* 141, 1–5. doi:10.1016/j.gexplo.2014.03.022

Camboa L. A. P., and Rabinowitz P. D. (1984). The Evolution of the Rio Grande Rise in the Southwest Atlantic Ocean. *Mar. Geology.* 58, 35–58. doi:10.1016/0025-3227(84)90115-4

Capobianco C. J., and Drake M. J. (1990). Partitioning of Ruthenium, Rhodium, and Palladium between Spinel and Silicate Melt and Implications for Platinum Group Element Fractionation Trends. *Geochimica et Cosmochimica Acta* 54, 869–874. doi:10.1016/0016-7037(90)90379-y

Chang W.-C. (1983). On Using Principal Components before Separating a Mixture of Two Multivariate Normal Distributions. *Appl. Stat.* 32, 267–275. doi:10.2307/2347949

Chassé M., Griffin W. L., Alard O., O'Reilly S. Y., and Calas G. (2018). Insights into the Mantle Geochemistry of Scandium from a Meta-Analysis of Garnet Data. *Lithos* 310-311, 409–421. doi:10.1016/j.lithos.2018.03.026

Chayes F. (1960). On Correlation between Variables of Constant Sum. *J. Geophys. Res.* 65 (12), 4185–4193. doi:10.1029/jz065i012p04185

Choi E., Fiorentini M. L., Hughes H. S. R., and Giuliani A. (2020). Platinum-group Element and Au Geochemistry of Late Archean to Proterozoic Calc-Alkaline and Alkaline Magmas in the Yilgarn Craton, Western Australia. *Lithos* 374-375, 105716. doi:10.1016/j.lithos.2020.105716

Courtillot V., Davaille A., Besse J., and Stock J. (2003). Three Distinct Types of Hotspots in the Earth's Mantle. *Earth Planet. Sci. Lett.* 205, 295–308. doi:10.1016/S0012-821X(02)01048-8

Cox K. G., Bell J. D., and Pankhurst R. J. (1979). *The Interpretation of Igneous Rocks*. London: George, Allen and Ulwin.

Davies D. L., and Bouldin D. W. (1979). "A Cluster Separation Measure," in *IEEE Trans. Pattern Anal. Mach. Intell.* (IEEE), 224–227. doi:10.1109/tpami.1979.4766909

Davis J. C. (2002). *Statistics and Data Analysis in Geology*. 3rd ed. John Wiley & Sons.

de Wit M. J., Stankiewicz J., and Reeves C. (2008). Restoring Pan-African-Brasiliano Connections: More Gondwana Control, Less Trans-Atlantic Corruption. *Geol. Soc. Lond. Spec. Publications* 294, 399–412. doi:10.1144/SP294.20

Der Verfasser A., Behrmann J. H., Shulgin A., and Prokoph A. (2011). High Resolution Bathymetric Survey on the NW Slope of Walvis Ridge, Offshore Namibia. *Berichte der Naturforschenden Gesellschaft zu Freibg. I. Br.* 101, 97–110.

Douglass J., Schilling J.-G., and Fontignie D. (1999). Plume-ridge Interactions of the Discovery and Shona Mantle Plumes with the Southern Mid-Atlantic Ridge (40˚-55˚S). *J. Geophys. Res.* 104, 2941–2962. doi:10.1029/98jb02642

Erlank A. J., Marsh J. S., Duncan A. R., Miller R. M., Hawkesworth C. J., Betton P. J., et al. (1984). Geochemistry and Petrogenesis of the Etendeka Volcanic Rocks from South West Africa/Namibia. *Geol. Soc. South. Afr. Spec. Publ.* 13, 195–246.

Ewart A., Milner S. C., Armstrong R. A., and Duncan A. R. (1998b). Etendeka Volcanism of the Goboboseb Mountains and Messum Igneous Complex, Namibia. Part II: Voluminous Quartz Latite Volcanism of the Awahab Magma System. *J. Pet.* 39, 227–253. doi:10.1093/petroj/39.2.227

Ewart A., Milner S. C., Armstrong R. A., and Dungan A. R. (1998a). Etendeka Volcanism of the Goboboseb Mountains and Messum Igneous Complex, Namibia. Part I: Geochemical Evidence of Early Cretaceous Tristan Plume Melts and the Role of Crustal Contamination in the Parana-Etendeka CFB. *J. Pet.* 39, 191–225. doi:10.1093/petroj/39.2.191

Ewart A. (2004). Petrology and Geochemistry of Early Cretaceous Bimodal Continental Flood Volcanism of the NW Etendeka, Namibia. Part 1: Introduction, Mafic Lavas and Re-evaluation of Mantle Source Components. *J. Pet.* 45, 59–105. doi:10.1093/petrology/egg083

Fodor R. V. (1987). Low- and High-TiO2 Flood Basalts of Southern Brazil: Origin from Picritic Parentage and a Common Mantle Source. *Earth Planet. Sci. Lett.* 84, 423–430. doi:10.1016/0012-821X(87)90007-0

Fodor R. V., McKee E. H., and Roisenberg A. (1989). Age Distribution of Serra Geral (Paraná) Flood Basalts, Southern Brazil. *J. South Am. Earth Sci.* 2, 343–349. doi:10.1016/0895-9811(89)90012-6

Fromm T., Jokat W., and Behrmann J. H. (2017). Interaction between a Hotspot and a Fracture Zone: The Crustal Structure of Walvis Ridge at 6˚ E. *Tectonophysics* 716, 108–120. doi:10.1016/j.tecto.2017.03.001

Fromm T., Planert L., Jokat W., Ryberg T., Behrmann J. H., Weber M. H., et al. (2015). South Atlantic Opening: A Plume-Induced Breakup? *Geology* 43, 931–934. doi:10.1130/g36936.1

Gallagher K., and Hawkesworth C. (1994). Mantle Plumes, continental Magmatism and Asymmetry in the South Atlantic. *Earth Planet. Sci. Lett.* 123, 105–117. doi:10.1016/0012-821x(94)90261-5

Garland F., Hawkesworth C. J., and Mantovani M. S. M. (1995). Description and Petrogenesis of the Paran Rzhyolites, Southern Brazil. *J. Pet.* 36, 1193–1227. doi:10.1093/petrology/36.5.1193

Gibson S. A., Thompson R. N., Day J. A., Humphris S. E., and Dickin A. P. (2005). Melt-generation Processes Associated with the Tristan Mantle Plume: Constraints on the Origin of EM-1. *Earth Planet. Sci. Lett.* 237, 744–767. doi:10.1016/j.epsl.2005.06.015

Gibson S. A., Thompson R. N., Leonardos O. H., Dickin A. P., and Mitchell J. G. (1999). The Limited Extent of Plume-Lithosphere Interactions during continental Flood-basalt Genesis: Geochemical Evidence from Cretaceous Magmatism in Southern Brazil. *Contrib. Mineralogy Pet.* 137, 147–169. doi:10.1007/s004100050588

Gomes A. S., Licht O. A. B., Vasconcellos E. M. G., and Soares J. S. (2018). Chemostratigraphy and Evolution of the Paraná Igneous Province Volcanism in the central Portion of the State of Paraná, Southern Brazil. *J. Volcanology Geothermal Res.* 355, 253–269. doi:10.1016/j.jvolgeores.2017.09.002

Gordon J. M. (1947). "Classification of the Gondwanic Rocks of Paraná, Santa Catarina and Rio Grande Do Sul. Rio de," in *Dept. Nac. Prod. Min., Div. Geol. e Min., Notas Prelim*, 1–19.

Graça M. C., Kusznir N., and Gomes Stanton N. S. (2019). Crustal Thickness Mapping of the central South Atlantic and the Geodynamic Development of the Rio Grande Rise and Walvis Ridge. *Mar. Pet. Geology.* 101, 230–242. doi:10.1016/j.marpetgeo.2018.12.011

Griffin W. L., Begg G. C., and O'Reilly S. Y. (2013). Continental-root Control on the Genesis of Magmatic Ore Deposits. *Nat. Geosci.* 6, 905–910. doi:10.1038/ngeo1954

Griffiths R. W., and Campbell I. H. (1990). Stirring and Structure in Mantle Starting Plumes. *Earth Planet. Sci. Lett.* 99, 66–78. doi:10.1016/0012-821x(90)90071-5

Handler M. R., and Bennett V. C. (1999). Behaviour of Platinum-Group Elements in the Subcontinental Mantle of Eastern Australia during Variable Metasomatism and Melt Depletion. *Geochimica et Cosmochimica Acta* 63, 3597–3618. doi:10.1016/s0016-7037(99)00143-x

Harris C. R., Millman K. J., van der Walt S. J., Gommers R., Virtanen P., Cournapeau D., et al. (2020). Array Programming with NumPy. *Nature* 585, 357–362. doi:10.1038/s41586-020-2649-2

Hartmann L. A., Baggio S. B., Brückmann M. P., Knijnik D. B., Lana C., Massonne H.-J., et al. (2019). U-pb Geochronology of Paraná Volcanics Combined with Trace Element Geochemistry of the Zircon Crystals and Zircon Hf Isotope Data. *J. South Am. Earth Sci.* 89, 219–226. doi:10.1016/j.jsames.2018.11.026

Hastie T., Tibshirani R., and Friedman J. (2009). *The Elements of Statistical Learning: Data Mining, Inference, and Prediction*. 2nd ed. Springer.

Hawkesworth C., Mantovani M., and Peate D. (1988). Lithosphere Remobilization during Parana CFB Magmatism. *J. Pet.* Special_Volume, 205–223. doi:10.1093/petrology/special_volume.1.205

Hawkesworth C., and Scherstén A. (2007). Mantle Plumes and Geochemistry. *Chem. Geology.* 241, 319–331. doi:10.1016/j.chemgeo.2007.01.018

Helmy H. M., and Bragagni A. (2017). Platinum-group Elements Fractionation by Selective Complexing, the Os, Ir, Ru, Rh-Arsenide-Sulfide Systems above 1020 ˚C. *Geochimica et Cosmochimica Acta* 216, 169–183. doi:10.1016/j.gca.2017.01.040

Hoernle K., Rohde J., Hauff F., Garbe-Schönberg D., Homrighausen S., Werner R., et al. (2015). How and when Plume Zonation Appeared during the 132 Myr Evolution of the Tristan Hotspot. *Nat. Commun.* 6, 7799. doi:10.1038/ncomms8799

Holwell D. A., Fiorentini M., McDonald I., Lu Y., Giuliani A., Smith D. J., et al. (2019). A Metasomatized Lithospheric Mantle Control on the Metallogenic Signature of post-subduction Magmatism. *Nat. Commun.* 10, 1–10. doi:10.1038/s41467-019-11065-4

Holzheid A., Sylvester P., O'Neill H. S. C., Rubie D. C., and Palme H. (2000). Evidence for a Late Chondritic Veneer in the Earth's Mantle from High-Pressure Partitioning of Palladium and Platinum. *Nature* 406, 396–399. doi:10.1038/35019050

Homrighausen S., Hoernle K., Hauff F., Wartho J.-A., van den Bogaard P., and Garbe-Schönberg D. (2019). New Age and Geochemical Data from the Walvis Ridge: The Temporal and Spatial Diversity of South Atlantic Intraplate Volcanism and its Possible Origin. *Geochimica et Cosmochimica Acta* 245, 16–34. doi:10.1016/j.gca.2018.09.002

Horrocks T., Holden E.-J., Wedge D., Wijns C., and Fiorentini M. (2019). Geochemical Characterisation of Rock Hydration Processes Using T-SNE. *Comput. Geosciences* 124, 46–57. doi:10.1016/j.cageo.2018.12.005

Hotelling H. (1933). Analysis of a Complex of Statistical Variables into Principal Components. *J. Educ. Psychol.* 24, 417–441. doi:10.1037/h0071325

Howarth R. J. (1983). "Statistics and Data Analysis in Geochemical Prospecting," in *Handbook of Exploration Geochemistry*. Editor G. J. S. Govett (Amsterdam: Elsevier).

Huber H., Koeberl C., McDonald I., and Reimold W. U. (2001). Geochemistry and Petrology of Witwatersrand and Dwyka Diamictites from south Africa: Search for an Extraterrestrial Component. *Geochimica et Cosmochimica Acta* 65, 2007–2016. doi:10.1016/s0016-7037(01)00569-5

Hughes H. S. R., McDonald I., Goodenough K. M., Ciborowski T. J. R., Kerr A. C., Davies J. H. F. L., et al. (2014). Enriched Lithospheric Mantle Keel below the Scottish Margin of the North Atlantic Craton: Evidence from the Palaeoproterozoic Scourie Dyke Swarm and

Mantle Xenoliths. *Precambrian Res.* 250, 97–126. doi:10.1016/j.precamres.2014.05.026

Hughes H. S. R., McDonald I., and Kerr A. C. (2015). Platinum-group Element Signatures in the North Atlantic Igneous Province: Implications for Mantle Controls on Metal Budgets during continental Breakup. *Lithos* 233, 89–110. doi:10.1016/j.lithos.2015.05.005

Hughes H. S. R., McDonald I., Loocke M., Butler I. B., Upton B. G. J., and Faithfull J. W. (2017). Paradoxical Co-existing Base Metal Sulphides in the Mantle: The Multi-Event Record Preserved in Loch Roag Peridotite Xenoliths, North Atlantic Craton. *Lithos* 276, 103–121. doi:10.1016/j.lithos.2016.09.035

Hyvärinen A., Karhunen J., and Oja E. (2001). "Introduction," in *Independent Component Analysis*. Editor S. Haykin (New York: John Wiley & Sons).

Jellinek A. M., and Manga M. (2004). Links between Long-Lived Hot Spots, Mantle Plumes, D", and Plate Tectonics. *Rev. Geophys.* 42, 1–35. doi:10.1029/2003rg000144

Jennings E. S., Gibson S. A., Maclennan J., and Heinonen J. S. (2017). Deep Mixing of Mantle Melts beneath continental Flood basalt Provinces: Constraints from Olivine-Hosted Melt Inclusions in Primitive Magmas. *Geochimica et Cosmochimica Acta* 196, 36–57. doi:10.1016/j.gca.2016.09.015

Jennings E. S., Gibson S. A., and Maclennan J. (2019). Hot Primary Melts and Mantle Source for the Paraná-Etendeka Flood basalt Province: New Constraints from Al-In-Olivine Thermometry. *Chem. Geology.* 529, 119287. doi:10.1016/j.chemgeo.2019.119287

Jokat W., and Reents S. (2017). Hotspot Volcanism in the Southern South Atlantic: Geophysical Constraints on the Evolution of the Southern Walvis Ridge and the Discovery Seamounts. *Tectonophysics* 716, 77–89. doi:10.1016/j.tecto.2016.12.011

Jolliffe I. T. (2002). *Principal Component Analysis*. 2nd ed. New York: Springer.

Kellogg L. H., and King S. D. (1993). Effect of Mantle Plumes on the Growth of D" by Reaction between the Core and Mantle. *Geophys. Res. Lett.* 20, 379–382. doi:10.1029/93gl00045

Kreyszig E. (1979). *Advanced Engineering Mathematics*. 4th ed. Wiley.

Kullback S., and Leibler R. A. (1959). *Information Theory and Statistics*. 3rd ed. John Wiley & Sons. Available at: http://arxiv.org/abs/1706.01538.

Kuno H. (1968). "Differentiation of basalt Magmas," in *Basalts: The Poldervaart Treatsie on Rocks of Basaltic Composition* (Interscience), 623–688.

Kystol J., and Larsen L. M. (1999). *Analytical Procedures in the Rock Geochemical Laboratory of the Geological Survey of Denmark and Greenland*.

Le Roex A. P., Cliff R. A., and Adair B. J. I. (1990). Tristan da Cunha, South Atlantic: Geochemistry and Petrogenesis of a Basanite-Phonolite Lava Series. *J. Pet.* 31, 779–812. doi:10.1093/petrology/31.4.779

Le Roux P. J., Le Roex A. P., Schilling J.-G., Shimizu N., Perkins W. W., and Pearce N. J. G. (2002). Mantle Heterogeneity beneath the Southern Mid-Atlantic Ridge: Trace Element Evidence for Contamination of Ambient Asthenospheric Mantle. *Earth Planet. Sci. Lett.* 203, 479–498. doi:10.1016/s0012-821x(02)00832-4

Leinz V., Bartorelli A., Sadowski G. R., and Isotta C. A. L. (1966). Sobre o comportamento Do trapp basaltico da Bacia Do Paraná. *Bol. da Soc. Bras. Geol.* 15, 79–91.

Leinz V. (1949). "Contribuição à Geologia dos Derrames Basálticos Do Sul Do Brasil," in *Bol. Fac. Filos. Ciênc. Let. Univ. São Paulo, Geol.*, 1. doi:10.11606/issn.2526-3862.bffcluspgeologia.1949.121703Available at: http://www.revistas.usp.br/bffcluspgeologia/article/view/121703.

Licht O. A. B. (2018). A Revised Chemo-Chrono-Stratigraphic 4-D Model for the Extrusive Rocks of the Paraná Igneous Province. *J. Volcanology Geothermal Res.* 355, 32–54. doi:10.1016/j.jvolgeores.2016.12.003

Lightfoot P. C. (2007). Advances in Ni-Cu-PGE Sulphide Deposit Models and Implications for Exploration Technologies. *Ore Depos. Explor. Technol. Proc. Explor. 07 Decenn. Int. Conf. Miner. Explor.* 44, 629–646.

Lightfoot P. C., Hawkesworth C. J., Olshefsky K., Green T., Doherty W., and Keays R. R. (1997). Geochemistry of Tertiary Tholeiites and Picrites from Qeqertarssuaq (Disko Island) and Nuussuaq, West Greenland with Implications for the mineral Potential of Comagmatic Intrusions. *Contrib. Mineralogy Pet.* 128, 139–163. doi:10.1007/s004100050300

Lightfoot P. C., and Keays R. R. (2005). Siderophile and Chalcophile Metal Variations in Flood Basalts from the Siberian Trap, Noril'sk Region: Implications for the Origin of the Ni-Cu-PGE Sulfide Ores. *Econ. Geology.* 100 (3), 439–462. doi:10.2113/gsecongeo.100.3.439

Lindsay J. J., Hughes H. S. R., Yeomans C. M., Andersen J. C. Ø., and McDonald I. (2021a). A Machine Learning Approach for Regional Geochemical Data: Platinum-Group Element Geochemistry vs Geodynamic Settings of the North Atlantic Igneous Province. *Geosci. Front.* 12, 101098. doi:10.1016/j.gsf.2020.10.005

Lindsay J. J., Andersen J. C. O., Hughes H. S. R., McDonald I., Hastie A. R., Besser M. L., et al. (2021b). Platinum-Group Element Geochemistry of the Paraná Flood Basalts – Modelling Metallogenesis in Rifting Continental Plume Environments. *Geochim. Cosmochim. Acta* 311, 74–101. doi:10.1016/j.gca.2021.07.035

Lorand J.-P., and Alard O. (2001). Platinum-group Element Abundances in the Upper Mantle: New Constraints from *In Situ* and Whole-Rock Analyses of Massif central Xenoliths (France). *Geochimica et Cosmochimica Acta* 65, 2789–2806. doi:10.1016/s0016-7037(01)00627-5

Lorand J.-P., Luguet A., and Alard O. (2013). Platinum-group Element Systematics and Petrogenetic Processing of the continental Upper Mantle: A Review. *Lithos* 164-167, 2–21. doi:10.1016/j.lithos.2012.08.017

Lorand J.-P., Luguet A., and Alard O. (2008). Platinum-Group Elements: A New Set of Key Tracers for the Earth's Interior. *Elements* 4, 247–252. doi:10.2113/gselements.4.4.247

MacQueen J. (1967). Some Methods for Classification and Analysis of Multivariate Observations. *Proc. Fifth Berkeley Symp. Math. Stat. Probab.* 1, 281–297.

Maier W. D., Barnes S.-J., and Marsh J. S. (2003). The Concentrations of the noble Metals in Southern African Flood-type Basalts and MORB: Implications for Petrogenesis and Magmatic Sulphide Exploration. *Contrib. Mineralogy Pet.* 146, 44–61. doi:10.1007/s00410-003-0480-z

Maier W. D., and Groves D. I. (2011). Temporal and Spatial Controls on the Formation of Magmatic PGE and Ni-Cu Deposits. *Miner Deposita* 46, 841–857. doi:10.1007/s00126-011-0339-6

Mansur E. T., and Barnes S.-J. (2020). The Role of Te, as, Bi, Sn and Sb during the Formation of Platinum-Group-Element Reef Deposits: Examples from the Bushveld and Stillwater Complexes. *Geochimica et Cosmochimica Acta* 272, 235–258. doi:10.1016/j.gca.2020.01.008

Marques L. S., De Min A., Rocha-Júnior E. R. V., Babinski M., Bellieni G., and Figueiredo A. M. G. (2018). Elemental and Sr-Nd-Pb Isotope Geochemistry of the Florianópolis Dyke Swarm (Paraná Magmatic Province): Crustal Contamination and Mantle Source Constraints. *J. Volcanology Geothermal Res.* 355, 149–164. doi:10.1016/j.jvolgeores.2017.07.005

Marques L. S., Dupré B., and Piccirillo E. M. (1999). Mantle Source Compositions of the Parana Magmatic Province (Southern Brazil): Evidence from Trace Element and Sr-Nd-Pb Isotope Geochemistry. *J. Geodynamics* 28 (4–5), 439–458. doi:10.1016/S0264-3707(99)00020-4

Marsh J. S., Ewart A., Milner S. C., Duncan A. R., and Miller R. M. (2001). The Etendeka Igneous Province: Magma Types and Their Stratigraphic Distribution with Implications for the Evolution of

the Paraná-Etendeka Flood basalt Province. *Bull. Volcanol.* 62, 464–486. doi:10.1007/s004450000115

Marsland S. (2009). *Machine Learning an Algorithmic Perspective Second Edition*. 2nd ed. Boca Raton, FL: CRC Press.

Martins-Ferreira M. A. C., Dias A. N. C., Chemale F., and Campos J. E. G. (2020). Intracontinental Uplift of the Brazilian Central Plateau Linked to continental Breakup, Orogenies, and basin Filling, Supported by Apatite and Zircon Fission-Track Data. *Arab. J. Geosci.* 13, 1. doi:10.1007/s12517-020-05885-8

Mathieu L. (2018). Quantifying Hydrothermal Alteration: a Review of Methods. *Geosciences* 8, 1–27. doi:10.3390/geosciences8070245

McDonald I., and Viljoen K. S. (2006). Platinum-group Element Geochemistry of Mantle Eclogites: a Reconnaissance Study of Xenoliths from the Orapa Kimberlite, Botswana. *Appl. Earth Sci.* 115, 81–93. doi:10.1179/174327506X138904

McDonough W. F., and Sun S.-S. (1995). The Composition of the Earth. *Chem. Geology.* 120, 223–253. doi:10.1016/0009-2541(94)00140-4

McKenzie D., and White R. (1989). Magmatism at Rift Zones: The Generation of Volcanic continental Margins and Flood Basalts. *J. Geophys. Res.* 94, 7685–7729. doi:10.1029/JB094IB06P07685

McKinney W. (2010). Data Structures for Statistical Computing in Python. *Proc. 9th Python Sci. Conf.* 1, 56–61. doi:10.25080/majora-92bf1922-00a

Michie D., Spiegelhalter D. J., and Taylor C. C. (1994). *Machine Learning, Neural and Statistical Classification*. Ellise Horwood Limited.

Miller R. M. (2008). *The Geology of Namibia*. Windhoek, Namibia: Ministry of Mines and Energy, Geological Survey of Namibia.

Milner S. C., Duncan A. R., Ewart A., and Marsh J. S. (1995a). Promotion of the Etendeka Formation to Group Status: A New Integrated Stratigraphy. *Commun. Geol. Surv. Namib* 9, 5–11.

Milner S. C., Duncan A. R., Whittingham A. M., and Ewart A. (1995b). Trans-Atlantic Correlation of Eruptive Sequences and Individual Silicic Volcanic Units within the Paraná-Etendeka Igneous Province. *J. Volcanology Geothermal Res.* 69, 137–157. doi:10.1016/0377-0273(95)00040-2

Milner S. C., Le Roex A. P., and O'Connor J. M. (1995c). Age of Mesozoic Igneous Rocks in northwesternNamibia, and Their Relationship to continental Breakup. *J. Geol. Soc.* 152, 97–104. doi:10.1144/gsjgs.152.1.0097

Mitchell R. H., and Keays R. R. (1981). Abundance and Distribution of Gold, Palladium and Iridium in Some Spinel and Garnet Lherzolites: Implications for the Nature and Origin of Precious Metal-Rich Intergranular Components in the Upper Mantle. *Geochimica et Cosmochimica Acta* 45, 2425–2442. doi:10.1016/0016-7037(81)90096-x

Momme P., Óskarsson N. x. e., and Keays R. R. (2003). Platinum-group Elements in the Icelandic Rift System: Melting Processes and Mantle Sources beneath Iceland. *Chem. Geology.* 196, 209–234. doi:10.1016/S0009-2541(02)00414-X

Momme P., Tegner C., Brooks C. K., and Keays R. R. (2006). Two Melting Regimes during Paleogene Flood basalt Generation in East Greenland: Combined REE and PGE Modelling. *Contrib. Mineral. Petrol.* 151, 88–100. doi:10.1007/s00410-005-0047-2

Momme P., Tegner C., Brooks K., and Keays R. (2002). The Behaviour of Platinum-Group Elements in Basalts from the East Greenland Rifted Margin. *Contrib. Mineralogy Pet.* 143, 133–153. doi:10.1007/s00410-001-0338-1

Morgan W. J. (1971). Convection Plumes in the Lower Mantle. *Nature* 230, 42–43. doi:10.1038/230042a0

Morgan W. J. (1972). Deep Mantle Convection Plumes and Plate Motions. *Am. Assoc. Pet. Geol. Bull.* 56, 203–213. doi:10.1306/819a3e50-16c5-11d7-8645000102c1865d

Naldrett A. J. (1997). Key Factors in the Genesis of Noril'sk, Sudbury, Jinchuan, Voisey's Bay and Other World-class Ni-Cu-PGE Deposits: Implications for Exploration. *Aust. J. Earth Sci.* 44, 283–315. doi:10.1080/08120099708728314

Natali C., Beccaluva L., Bianchini G., and Siena F. (2017). Comparison Among Ethiopia-Yemen, Deccan, and Karoo continental Flood Basalts of central Gondwana: Insights on Lithosphere versus Asthenosphere Contributions in Compositionally Zoned Magmatic Provinces. *Spec. Pap. Geol. Soc. Am.* 526, 191–215. doi:10.1130/2017.2526(10)

Nielsen T. F. D., Andersen J. C. Ø., Holness M. B., Keiding J. K., Rudashevsky N. S., Rudashevsky V. N., et al. (2014). The Skaergaard PGE and Gold deposit: The Result of *In Situ* Fractionation, Sulphide Saturation, and Magma Chamber-Scale Precious Metal Redistribution by Immiscible Fe-Rich Melt. *J. Petrol.* 56, 1643–1676. doi:10.1093/petrology/egv049

O'Connor J. M., and Duncan R. A. (1990). Evolution of the Walvis Ridge-Rio Grande Rise Hot Spot System: Implications for African and South American Plate Motions over Plumes. *J. Geophys. Res.* 95, 17475. doi:10.1029/JB095iB11p17475

O'Connor J. M., and Jokat W. (2015). Tracking the Tristan-Gough Mantle Plume Using Discrete Chains of Intraplate Volcanic Centers Buried in the Walvis Ridge. *Geology* 43, 715–718. doi:10.1130/G36767.1

O'Driscoll B., Butcher A. R., and Latypov R. (2014). New Insights into Precious Metal Enrichment on the Isle of Rum. *Scotland.* Geol. Today 30, 134–141. doi:10.1111/gto.12059

Palowsky-Glahn V., and Egozcue J. J. (2006). Compositional Data and Their Analysis: An Introduction. *Geol. Soc. Spec. Publications* 264 (1), 1–10. doi:10.1144/GSL.SP.2006.264.01.01

Park J.-W., Kamenetsky V., Campbell I., Park G., Hanski E., and Pushkarev E. (2017). Empirical Constraints on Partitioning of Platinum Group Elements between Cr-Spinel and Primitive Terrestrial Magmas. *Geochimica et Cosmochimica Acta* 216, 393–416. doi:10.1016/j.gca.2017.05.039

Peach C. L., Mathez E. A., Keays R. R., and Reeves S. J. (1994). Experimentally Determined Sulfide Melt-Silicate Melt Partition Coefficients for Iridium and Palladium. *Chem. Geology.* 117, 361–377. doi:10.1016/0009-2541(94)90138-4

Pearce J. A. (2008). Geochemical Fingerprinting of Oceanic Basalts with Applications to Ophiolite Classification and the Search for Archean Oceanic Crust. *Lithos* 100, 14–48. doi:10.1016/j.lithos.2007.06.016

Pearson K. (1901). LIII. On Lines and Planes of Closest Fit to Systems of Points in Space. *Lond. Edinb. Dublin Phil. Mag. J. Sci.* 2, 559–572. doi:10.1080/14786440109462720

Peate D. W., and Hawkesworth C. J. (1996). Lithospheric to Asthenospheric Transition in Low-Ti Flood Basalts from Southern Paraná, Brazil. *Chem. Geology.* 127, 1–24. doi:10.1016/0009-2541(95)00086-0

Peate D. W., Hawkesworth C. J., and Mantovani M. S. M. (1992). Chemical Stratigraphy of the Paraná Lavas (South America): Classification of Magma Types and Their Spatial Distribution. *Bull. Volcanol.* 55, 119–139. doi:10.1007/bf00301125

Peate D. W., Hawkesworth C. J., Mantovani M. S. M., and Shukowsky W. (1990). Mantle Plumes and Flood-basalt Stratigraphy in the Paraná, South America. *Geol.* 18, 1223–1226. doi:10.1130/0091-7613(1990)018<1223:mpafbs>2.3.co;2

Peate D. W. (1997). The Paraná-Etendeka Province. *Geophys. Monogr. Ser. Ser.* 100, 217–245. doi:10.1029/GM100p0217

Pedregosa F., Varoquaux G., Gramfort A., Michel V., Thirion B., Grisel O., et al. (2011). Scikit-learn: Machine Learning in Python. *J. Ma* 12, 2825–2830.

Philipp H., Eckhardt J.-D., and Puchelt H. (2001). Platinum-Group Elements (PGE) in Basalts of the Seaward-Dipping Reflector Sequence, SE Greenland Coast. *J. Petrol.* 42, 407–432. doi:10.1093/petrology/42.2.407

Piccirillo E. M., Melfi A. J., Comin-Chiaramonti P., Bellieni G., Ernesto M., Marques L. S., et al. (1988). "Continental Flood Volcanism from the Paraná Basin (Brazil)," in *Continental Flood Basalts*. Editor J. D. McDougall (London: Chapman and Hall), 195–238.

Pirrie D., Power M. R., Andersen J. C. Ø., and Butcher a. R. (2000). Platinum-group Mineralization in the Tertiary Igneous Province: New Data from Mull and Skye, Scottish Inner Hebrides, UK. *Geol. Mag.* 137, 651–658. doi:10.1017/s0016756800004520

Pitcher L., Helz R. T., Walker R. J., and Piccoli P. (2009). Fractionation of the Platinum-Group Elments and Re during Crystallization of basalt in Kilauea Iki Lava Lake, Hawaii. *Chem. Geology.* 260, 196–210. doi:10.1016/j.chemgeo.2008.12.022

Polo L. A., Giordano D., Janasi V. A., and Guimarães L. F. (2018). Effusive Silicic Volcanism in the Paraná Magmatic Province, South Brazil: Physico-Chemical Conditions of Storage and Eruption and Considerations on the Rheological Behavior during Emplacement. *J. Volcanology Geothermal Res.* 355, 115–135. doi:10.1016/j.jvolgeores.2017.05.027

Powell W., and O'Reilly S. (2007). Metasomatism and Sulfide Mobility in Lithospheric Mantle beneath Eastern Australia: Implications for Mantle Re-os Chronology. *Lithos* 94, 132–147. doi:10.1016/j.lithos.2006.06.010

Power M. R., Pirrie D., Andersen J. C. Ø., and Wheeler P. D. (2000). Testing the Validity of Chrome Spinel Chemistry as a Provenance and Petrogenetic Indicator. *Geology* 28, 1027–1030. doi:10.1130/0091-7613(2000)028<1027:ttvocs>2.3.co;2

Rämö O. T., Heikkilä P. A., and Pulkkinen A. H. (2016). Geochemistry of Paraná-Etendeka Basalts from Misiones, Argentina: Some New Insights into the Petrogenesis of High-Ti continental Flood Basalts. *J. South Am. Earth Sci.* 67, 25–39. doi:10.1016/j.jsames.2016.01.008

Rehkämper M., Halliday A. N., Barfod D., Fitton J. G., and Dawson J. B. (1997). Platinum-group Element Abundance Patterns in Different Mantle Environments. *Science* 80-278, 1595–1598. doi:10.1126/science.278.5343.1595

Renne P. R., Glen J. M., Milner S. C., and Duncan A. R. (1996). Age of Etendeka Flood Volcanism and Associated Intrusions in Southwestern Africa. *Geol.* 24, 659–662. doi:10.1130/0091-7613(1996)024<0659:aoefva>2.3.co;2

Richter D. H., and Moore J. G. (1966). Petrology of the Kilauea Iki Lava lake, Hawaii. *U.S. Geol. Surv. Prof. Paper* 537-B, B1–B26. doi:10.3133/pp537b

Rielli A., Tomkins A. G., Nebel O., Raveggi M., Jeon H., Martin L., et al. (2018). Sulfur Isotope and PGE Systematics of Metasomatised Mantle Wedge. *Earth Planet. Sci. Lett.* 497, 181–192. doi:10.1016/j.epsl.2018.06.012

Righter K., Humayun M., and Danielson L. (2008). Partitioning of Palladium at High Pressures and Temperatures during Core Formation. *Nat. Geosci.* 1, 321–323. doi:10.1038/ngeo180

Ripley E. M., Lightfoot P. C., Li C., and Elswick E. R. (2003). Sulfur Isotopic Studies of continental Flood Basalts in the Noril'sk Region: Implications for the Association between Lavas and Ore-Bearing Intrusions. *Geochimica et Cosmochimica Acta* 67 (15), 2805–2817. doi:10.1016/s0016-7037(03)00102-9

Rocha-Júnior E. R. V., Marques L. S., Babinski M., Nardy A. J. R., Figueiredo A. M. G., and Machado F. B. (2013). Sr-Nd-Pb Isotopic Constraints on the Nature of the Mantle Sources Involved in the Genesis of the High-Ti Tholeiites from Northern Paraná Continental Flood Basalts (Brazil). *J. South Am. Earth Sci.* 46, 9–25. doi:10.1016/j.jsames.2013.04.004

Rocha-Júnior E. R. V., Puchtel I. S., Marques L. S., Walker R. J., Machado F. B., Nardy A. J. R., et al. (2012). Re-Os Isotope and Highly Siderophile Element Systematics of the Paraná continental Flood Basalts (Brazil). *Earth Planet. Sci. Lett.* 337-338, 164–173. doi:10.1016/j.epsl.2012.04.050

Rohde J., Hoernle K., Hauff F., Werner R., O'Connor J., Class C., et al. (2013b). 70 Ma Chemical Zonation of the Tristan-Gough Hotspot Track. *Geology* 41, 335–338. doi:10.1130/g33790.1

Rohde J. K., van den Bogaard P., Hoernle K., Hauff F., and Werner R. (2013a). Evidence for an Age Progression along the Tristan-Gough Volcanic Track from New 40Ar/39Ar Ages on Phenocryst Phases. *Tectonophysics* 604, 60–71. doi:10.1016/j.tecto.2012.08.026

Rollinson H. R. (1993). *Using Geochemical Data*. Abingdon-on-Thames, Oxfordshire: Routledge, 352.

Rossetti L., Lima E. F., Waichel B. L., Hole M. J., Simões M. S., and Scherer C. M. S. (2018). Lithostratigraphy and Volcanology of the Serra Geral Group, Paraná-Etendeka Igneous Province in Southern Brazil: Towards a Formal Stratigraphical Framework. *J. Volcanology Geothermal Res.* 355, 98–114. doi:10.1016/j.jvolgeores.2017.05.008

Shannon M. C., and Agee C. B. (1998). Percolation of Core Melts at Lower Mantle Conditions. *Sci. New Ser.* 280, 1059–1061. doi:10.1126/science.280.5366.1059

Simões M. S., Lima E. F., Rossetti L. M. M., and Sommer C. A. (2019). The Low-Ti High-Temperature Dacitic Volcanism of the Southern Paraná-Etendeka LIP: Geochemistry, Implications for Trans-Atlantic Correlations and Comparison with Other Phanerozoic LIPs. *Lithos* 342-343, 187–205. doi:10.1016/j.lithos.2019.05.030

Stewart K., Turner S., Kelley S., Hawkesworth C., Kirstein L., and Mantovani M. (1996). 3-D, 40Ar-39Ar Geochronology in the Paraná continental Flood basalt Province. *Earth Planet. Sci. Lett.* 143, 95–109. doi:10.1016/0012-821X(96)00132-X

Stracke A., Hofmann A. W., and Hart S. R. (2005). FOZO, HIMU, and the Rest of the Mantle Zoo. *Geochemistry, Geophys. Geosystems* 6, 1. doi:10.1029/2004gc000824

Stroncik N. A., Trumbull R. B., Krienitz M.-S., Niedermann S., Romer R. L., Harris C., et al. (2017). Helium Isotope Evidence for a Deep-Seated Mantle Plume Involved in South Atlantic Breakup. *Geology* 45, 827–830. doi:10.1130/g39151.1

Tassara S., González-Jiménez J. M., Reich M., Schilling M. E., Morata D., Begg G., et al. (2017). Plume-subduction Interaction Forms Large Auriferous Provinces. *Nat. Commun.* 8, 843–847. doi:10.1038/s41467-017-00821-z

Taylor G. J., Martel L. M. V., Karunatillake S., Gasnault O., and Boynton W. V. (2010). Mapping Mars Geochemically. *Geology* 38, 183–186. doi:10.1130/g30470.1

Tegner C., Thy P., Holness M. B., Jakobsen J. K., and Lesher C. E. (2009). Differentiation and Compaction in the Skaergaard Intrusion. *J. Petrol.* 50, 813–840. doi:10.1093/petrology/egp020

Teklay M., Wirth K., Mezger K., and Thole J. (2020). Picrites of the Jungfrau and Sargdeckel, central Namibia: Relative Roles of Mantle and Crust in the Southern Etendeka Large Igneous Province. *Lithos* 354-355, 105283. doi:10.1016/j.lithos.2019.105283

Thiede D. S., and Vasconcelos P. M. (2010). Paraná Flood Basalts: Rapid Extrusion Hypothesis Confirmed by New 40Ar/39Ar Results. *Geology* 38, 747–750. doi:10.1130/g30919.1

Thompson R. N., and Gibson S. A. (1991). Subcontinental Mantle Plumes, Hotspots and Pre-existing Thinspots. *J. Geol. Soc.* 148, 973–977. doi:10.1144/gsjgs.148.6.0973

Turner S., Hawkesworth C., Gallagher K., Stewart K., Peate D., and Mantovani M. (1996). Mantle Plumes, Flood Basalts, and thermal Models for Melt Generation beneath Continents: Assessment of a Conductive Heating Model and Application to the Paraná. *J. Geophys. Res.* 101, 11503–11518. doi:10.1029/96JB00430

Turner S. P., Peate D. W., Hawkesworth C. J., and Mantovani M. S. M. (1999). Chemical Stratigraphy of the Paraná basalt Succession in Western Uruguay: Further Evidence for the Diachronous Nature of the Paraná Magma Types. *J. Geodynamics* 28, 459–469. doi:10.1016/s0264-3707(99)00021-6

Ussami N., Chaves C. A. M., Marques L. S., and Ernesto M. (2013). Origin of the rio grande Rise-Walvis ridge Reviewed Integrating Palaeogeographic Reconstruction, Isotope Geochemistry and Flexural Modelling. *Geol. Soc. Lond. Spec. Publications* 369, 129–146. doi:10.1144/sp369.10

van der Maaten L. (2014). Accelerating T-SNE Using Tree-Based Algorithms. *J. Mach. Learn. Res.* 15, 3221–3245.

van der Maaten L., and Hinton G. (2008). Visualizing Data Using T-SNE. *J. Mach. Learn. Res.* 9, 2579–2605.

Wade C. E., Payne J. L., Barovich K. M., and Reid A. J. (2019). Heterogeneity of the Sub-continental Lithospheric Mantle and 'non-Juvenile' Mantle Additions to a Proterozoic Silicic Large Igneous Province. *Lithos* 340-341, 34087–341107. doi:10.1016/j.lithos.2019.05.005

Wang J., Zhou Y., and Xiao F. (2020b). Identification of Multi-Element Geochemical Anomalies Using Unsupervised Machine Learning

Algorithms: A Case Study from Ag-Pb-Zn Deposits in north-western Zhejiang, China. *Appl. Geochem.* 120, 104679. doi:10.1016/j.apgeochem.2020.104679

Wang Z., Cheng H., Zong K., Geng X., Liu Y., Yang J., et al. (2020a). Metasomatized Lithospheric Mantle for Mesozoic Giant Gold Deposits in the North China Craton. *Geology* 48, 169–173. doi:10.1130/g46662.1

Weaver B. L. (1991). The Origin of Ocean Island basalt End-Member Compositions: Trace Element and Isotopic Constraints. *Earth Planet. Sci. Lett.* 104, 381–397. doi:10.1016/0012-821x(91)90217-6

Weit A., Trumbull R. B., Keiding J. K., Geissler W. H., Gibson S. A., and Veksler I. V. (2017). The magmatic system beneath the Tristan da Cunha Island: Insights from thermobarometry, melting models and geophysics. *Tectonophysics* 716, 64–76. doi:10.1016/j.tecto.2016.08.010

Willbold M., and Stracke A. (2006). Trace Element Composition of Mantle End-Members: Implications for Recycling of Oceanic and Upper and Lower continental Crust. *Geochemistry, Geophys. Geosystems* 7, 1–30. doi:10.1029/2005gc001005

Wilson M. (1992). Magmatism and continental Rifting during the Opening of the South Atlantic Ocean: a Consequence of Lower Cretaceous Super-plume Activity? *Geol. Soc. Lond. Spec. Publications* 68, 241–255. doi:10.1144/GSL.SP.1992.068.01.15

Wilson M. R., Kyser T. K., and Fagan R. (1996). Sulfur Isotope Systematics and Platinum Group Element Behavior in REE-Enriched Metasomatic Fluids: A Study of Mantle Xenoliths from Dish Hill, California, USA. *Geochimica et Cosmochimica Acta* 60, 1933–1942. doi:10.1016/0016-7037(96)00069-5

Woodland A. B., Uenver-Thiele L., and Seitz H.-M. (2018). Influence of Metasomatism on Vanadium-Based Redox Proxies for Mantle Peridotite. *Geochem. Persp. Let.* 8, 11–16. doi:10.7185/geochemlet.1822

Woodland S. J., Pearson D. G., and Thirlwall M. F. (2002). A Platinum Group Element and Re-os Isotope Investigation of Siderophile Element Recycling in Subduction Zones: Comparison of Grenada, Lesser Antilles Arc, and the Izu-Bonin Arc. *J. Petrol.* 43, 171–198. doi:10.1093/petrology/43.1.171

Zhang M., O'Reilly S. Y., Wang K.-L., Hronsky J., and Griffin W. L. (2008). Flood Basalts and Metallogeny: The Lithospheric Mantle Connection. *Earth-Science Rev.* 86, 145–174. doi:10.1016/j.earscirev.2007.08.007

Zhou H., Hoernle K., Geldmacher J., Hauff F., Homrighausen S., Garbe-Schönberg D., et al. (2020). Geochemistry of Etendeka Magmatism: Spatial Heterogeneity in the Tristan-Gough Plume Head. *Earth Planet. Sci. Lett.* 535, 116123. doi:10.1016/j.epsl.2020.116123

Zindler A., and Hart S. (1986). Chemical Geodynamics. *Annu. Rev. Earth Planet. Sci.* 14, 493–571. doi:10.1146/annurev.ea.14.050186.002425